



# TURKISH JOURNAL OF ENGINEERING

## **EDITOR IN CHIEF**

*Prof. Dr. Murat YAKAR*  
Mersin University Engineering Faculty  
Turkey

## **CO-EDITORS**

*Prof. Dr. Erol YAŞAR*  
Mersin University Faculty of Art and Science  
Turkey

*Assoc. Prof. Dr. Cahit BİLİM*  
Mersin University Engineering Faculty  
Turkey

*Assist. Prof. Dr. Hüdaverdi ARSLAN*  
Mersin University Engineering Faculty  
Turkey

## **ADVISORY BOARD**

*Prof. Dr. Orhan ALTAN*  
Honorary Member of ISPRS, ICSU EB Member  
Turkey

*Prof. Dr. Armin GRUEN*  
ETH Zurich University  
Switzerland

*Prof. Dr. Hacı Murat YILMAZ*  
Aksaray University Engineering Faculty  
Turkey

*Prof. Dr. Artu ELLMANN*  
Tallinn University of Technology Faculty of Civil Engineering  
Estonia

*Assoc. Prof. Dr. E. Çağlan KUMBUR*  
Drexel University  
USA

## **TECHNICAL EDITORS**

*Prof. Dr. Ali AKDAĞLI*  
Dean of Engineering Faculty  
Turkey

*Prof. Dr. Roman KOCH*  
Erlangen-Nurnberg Institute Palaontologie  
Germany

*Prof. Dr. Hamdalla WANAS*  
Menoufyia University, Science Faculty  
Egypt

*Prof. Dr. Turgay CELIK*  
Witwatersrand University  
South Africa

*Prof. Dr. Muhsin EREN*  
Mersin University Engineering Faculty  
Turkey

*Prof. Dr. Johannes Van LEEUWEN*  
Iowa State University  
USA

*Prof. Dr. Elias STATHATOS*  
TEI of Western Greece  
Greece

*Prof. Dr. Vedamanickam SAMPATH*  
Institute of Technology Madras  
India

*Prof. Dr. Khandaker M. Anwar HOSSAIN*  
Ryerson University  
Canada

*Prof. Dr. Hamza EROL*  
Mersin University Engineering Faculty  
Turkey

*Prof. Dr. Ali Cemal BENİM*  
Duesseldorf University of Applied Sciences  
Germany

*Prof. Dr. Mohammad Mehdi RASHIDI*  
University of Birmingham  
England

*Prof. Dr. Muthana SHANSAL*  
Baghdad University  
Iraq

*Prof. Dr. Ibrahim S. YAHIA*  
Ain Shams University  
Egypt

*Assoc. Prof. Dr. Kurt A. ROSENTRATER*  
Iowa State University  
USA

*Assoc. Prof. Dr. Christo ANANTH*  
Francis Xavier Engineering College  
India

*Assoc. Prof. Dr. Bahadır K. KÖRBAHTI*  
Mersin University Engineering Faculty  
Turkey

*Assist. Prof. Dr. Akin TATOGLU*  
Hartford University College of Engineering  
USA

*Assist. Prof. Dr. Şevket DEMİRÇİ*  
Mersin University Engineering Faculty  
Turkey

*Assist. Prof. Dr. Yelda TURKAN*  
Oregon State University  
USA

*Assist. Prof. Dr. Gökhan ARSLAN*  
Mersin University Engineering Faculty  
Turkey

*Assist. Prof. Dr. Seval Hale GÜLER*  
Mersin University Engineering Faculty  
Turkey

*Assist. Prof. Dr. Mehmet ACI*  
Mersin University Engineering Faculty  
Turkey

*Dr. Ghazi DROUBI*  
Robert Gordon University Engineering Faculty  
Scotland, UK

#### **JOURNAL SECRETARY**

*Nida DEMİRTAŞ*  
nidademirtas@mersin.edu.tr

#### **TURKISH JOURNAL OF ENGINEERING (TUJE)**

Turkish Journal of Engineering (TUJE) is a multi-disciplinary journal. The Turkish Journal of Engineering (TUJE) publishes the articles in English and is being published 3 times (January, May, September) a year. The Journal is a multidisciplinary journal and covers all fields of basic science and engineering. It is the main purpose of the Journal that to convey the latest development on the science and technology towards the related scientists and to the readers. The Journal is also involved in both experimental and theoretical studies on the subject area of basic science and engineering. Submission of an article implies that the work described has not been published previously and it is not under consideration for publication elsewhere. The copyright release form must be signed by the corresponding author on behalf of all authors. All the responsibilities for the article belongs to the authors. The publications of papers are selected through double peer reviewed to ensure originality, relevance and readability.

#### **AIM AND SCOPE**

The Journal publishes both experimental and theoretical studies which are reviewed by at least two scientists and researchers for the subject area of basic science and engineering in the fields listed below:

- Aerospace Engineering
- Environmental Engineering
- Civil Engineering
- Geomatic Engineering
- Mechanical Engineering
- Geology Science and Engineering
- Mining Engineering
- Chemical Engineering
- Metallurgical and Materials Engineering
- Electrical and Electronics Engineering
- Mathematical Applications in Engineering
- Computer Engineering
- Food Engineering

#### **PEER REVIEW PROCESS**

All submissions will be scanned by iThenticate® to prevent plagiarism. Author(s) of the present study and the article about the ethical responsibilities that fit PUBLICATION ETHICS agree. Each author is responsible for the content of the article. Articles submitted for publication are priorly controlled via iThenticate ® (Professional Plagiarism Prevention) program. If articles that are controlled by iThenticate® program identified as plagiarism or self-plagiarism with more than 25% manuscript will return to the author for appropriate citation and correction. All submitted manuscripts are read by the editorial staff. To save time for authors and peer-reviewers, only those papers that seem most likely to meet our editorial criteria are sent for formal review. Reviewer selection is critical to the publication process, and we base our choice on many factors, including expertise, reputation, specific recommendations and our own previous experience of a reviewer's characteristics. For instance, we avoid using people who are slow, careless or do not provide reasoning for their views, whether harsh or lenient. All submissions will be double blind peer reviewed. All papers are expected to have original content. They should not have been previously published and it should not be under review. Prior to the sending out to referees, editors check that the paper aim and scope of the journal. The journal seeks minimum three independent referees. All submissions are subject to a double blind peer review; if two of referees gives a negative feedback on a paper, the paper is being rejected. If two of referees gives a positive feedback on a paper and one referee negative, the editor can decide whether accept or reject. All submitted papers and referee reports are archived by journal Submissions whether they are published or not are not returned. Authors who want to give up publishing their paper in TUJE after the submission have to apply to the editorial board in written. Authors are responsible from the writing quality of their papers. TUJE journal will not pay any copyright fee to authors. A signed Copyright Assignment Form has to be submitted together with the paper.

### **PUBLICATION ETHICS**

Our publication ethics and publication malpractice statement is mainly based on the Code of Conduct and Best-Practice Guidelines for Journal Editors. Committee on Publication Ethics (COPE). (2011, March 7). Code of Conduct and Best-Practice Guidelines for Journal Editors. Retrieved from [http://publicationethics.org/files/Code%20of%20Conduct\\_2.pdf](http://publicationethics.org/files/Code%20of%20Conduct_2.pdf)

### **PUBLICATION FREQUENCY**

The TUJE accepts the articles in English and is being published 3 times. January, May, September a year.

### **CORRESPONDENCE ADDRESS**

Journal Contact: [tuje@mersin.edu.tr](mailto:tuje@mersin.edu.tr)

# CONTENTS

*Volume 1 – Issue 2*

## ARTICLES

<b>MINERALOGICAL, GEOCHEMICAL AND MICROMORPHOLOGICAL CHARACTERISTICS OF CALCITE PRECIPITATED FROM A THIN COVER OF RECENT WATER TAKEN FROM THE STALAGMITES IN KÜPELİ CAVE, ESENPINAR (ERDEMLİ, MERSİN), SOUTHERN TURKEY</b> <i>Muhsin Eren, Selahattin Kadir and Murat Akgöz</i> .....	<b>44</b>
<b>REGRESSION MODELING OF THE HOLE QUALITIES DURING COLD WORK TOOL STEELS DRILLING, WITH DIFFERENT CHARACTERISTICS DRILL BITS</b> <i>İskender Özkul, Berat Barış Buldum and Adnan Akkurt</i> .....	<b>52</b>
<b>THE INVESTIGATION ON ELECTRICAL AND OPTICAL PROPERTIES OF CdO/CNT NANOCOMPOSITE</b> <i>Ömer Guler, M. Gökhan Albayrak, Mehmet Takgün and Seval Hale Güler</i> .....	<b>61</b>
<b>DESIGNING A COMPACT MONOPOLE MICROSTRIP ANTENNA OPERATING AT ULTRA-WIDE BAND FOR MICROWAVE IMAGING APPLICATIONS</b> <i>Mustafa Berkan Biçer and Ali Akdağlı</i> .....	<b>66</b>
<b>FABRICATION OF Cu-Al-Ni SHAPE MEMORY THIN FILM BY THERMAL EVAPORATION</b> <i>Canan Aksu Canbay, Ayşe Tekataş and İskender Özkul</i> .....	<b>70</b>
<b>DESIGN AND PROTOTYPE OF A COMPACT, ULTRA WIDE BAND DOUBLE RIDGED HORN ANTENNA FOR BEHIND OBSTACLE RADAR APPLICATIONS</b> <i>Betül Yılmaz and Caner Özdemir</i> .....	<b>76</b>
<b>PHOTOGRAMMETRIC MODELLING OF SAKAHANE MASJID USING AN UNMANNED AERIAL VEHICLE</b> <i>Ahmet Şasi, Murat Yakar</i> .....	<b>82</b>

# Turkish Journal of Engineering



*Turkish Journal of Engineering (TUJE)*  
*Vol. 1, Issue 2, pp. 44-51, September 2017*  
*ISSN 2587-1366, Turkey*  
*DOI: 10.31127/tuje.316859*  
*Research Article*

## **MINERALOGICAL, GEOCHEMICAL AND MICROMORPHOLOGICAL CHARACTERISTICS OF CALCITE PRECIPITATED FROM A THIN COVER OF RECENT WATER TAKEN FROM THE STALAGMITES IN KÜPELI CAVE, ESENPINAR (ERDEMLI, MERSIN), SOUTHERN TURKEY**

Muhsin Eren <sup>\*1</sup>, Selahattin Kadir <sup>2</sup> and Murat Akgöz <sup>3</sup>

<sup>1</sup>Mersin University, Engineering Faculty, Department of Geological Engineering, Mersin, Turkey  
(m\_eren@yahoo.com)

<sup>2</sup>Eskisehir Osmangazi University, Faculty of Engineering and Architecture, Department of Geological Engineering, Eskişehir, Turkey (skadir.esogu@gmail.com)

<sup>3</sup>General Directorate of Mineral Research and Exploration (MTA), Ankara, Turkey  
(murat\_akgoz@yahoo.com)

---

\* Corresponding Author

Received: 13/04/2017      Accepted: 16/05/2017

---

### **ABSTRACT**

Küpelı cave in southern Turkey (UTM: 36.606085 °N, 34.114917 °E, 742 m asl) shows recent stalagmite development at several points beneath dripping water on a stack of blocks due to collapse of the cave ceiling. Calcite precipitated from water supersaturated with respect to CaCO<sub>3</sub> under the surface conditions taken from a thin cover of water on the upper surface of stalagmites was analysed using the several analytical techniques, including XRD, DTA-TG, IR, ICP-OES and MS and stable isotope analyses. The results revealed that the precipitated material consists almost entirely of calcite. In the SEM images, the precipitate is composed mainly of euhedral to subhedral equant calcite crystals with size of 5-10 µm and an interwoven mass of calcite filaments. Stable isotope values of the calcite ( $\delta^{18}\text{O} = -3.81 \text{‰ V-PDB}$  and  $\delta^{13}\text{C} = -6.92 \text{‰ V-PDB}$ ) indicate precipitation from meteoric soil water. The crystalline fabric of the precipitate points out inorganic precipitation whereas filamentous forms suggest calcified green algae at advance stage of evaporation.

**Keywords:** *Newly Forming Calcite, Mineralogy, Micromorphology, Geochemistry, Küpelı Cave, Southern Turkey*

## 1. INTRODUCTION

Stalagmite is a type of speleothem that grows upward on the floor of a cave beneath dripping water. Cave deposits have received a great interest of researchers working on karst formation. Most studies mainly focus on stable isotope composition ( $\delta^{18}\text{O}$  and  $\delta^{13}\text{C}$ ) of cave calcite used for paleoclimatic reconstructions (e.g., Lauritzen and Lundberg, 1999; Vaks et al., 2003, 2010; McDermott, 2004; Johnson et al., 2006; Verheyden et al., 2008; Dominguez-Villar et al., 2008; Tremaine et al., 2011). Speleothems also provide information on soil/vegetation dynamics, hydrological conditions, annual lamination, growth rate and dating, organic acid contents and atmospheric changes (McDermott, 2004; Fairchild and Treble, 2009 and for other references). There is little information available considering recent cave deposits. Previous studies on recent speleothems focus on dating (Gascoyne and Nelson, 1983; Baskaran and Iliffe, 1993), growth rates (Baker and Smart, 1995; Baker et al., 1998; Genty et al., 2001; Sherwin and Baldini, 2011), factors affecting calcite growth and fabric (Turrero et al., 2009) and stable isotope composition (Riechelmann et al., 2013). In addition, Day and Henderson (2011) investigate oxygen isotope in calcite grown under cave-analogue conditions. Therefore, this study investigates mineralogy, geochemistry, stable isotope chemistry and micromorphology of newly forming calcite precipitated from a thin cover of water taken from the stalagmites, and provides some new data for recent cave deposits.

## 2. STUDY SETTING

### 2.1. Location and climate

Küpeli Cave is located at latitude 599726 E and longitude 4051941 N (UTM: 36.606085 °N, 34.114917 °E) and an elevation of 742 m in southern Turkey, about 1.7 km northeast of Esenpınar (Erdemli/Mersin; Figures 1, 2). This location takes a place within the Tauride orogenic belt where platform carbonates are common. Küpeli Cave was developed within the reefal limestone of the Mut Formation (Langian-Serravalian) in which red algae and corals are common (Figure 3; Gedik et al., 1979; Eren, 2008). Mediterranean-type semi-arid climate prevails at outside of the cave, characterized by the mean annual values of precipitation (634 mm), evaporation (1321 mm) and temperature (18.7 °C) obtained from the meteorological measurements of 70-years (Eren et al., 2008).

### 2.2. Geology

In the region, karstification is very common, and has been developed in carbonates at skirts of the Tauride Mountains where hundreds of caves including Küpeli Cave can be found with different features and processes (Akgöz and Eren, 2015). Karstification in the region probably started after emergence of the Central Taurides due to epirogenetic raise at the end of Miocene. Following the raise, karstification was deepened due to dry and hot climate. In the region, extension of karstic surface features and distribution of caves show

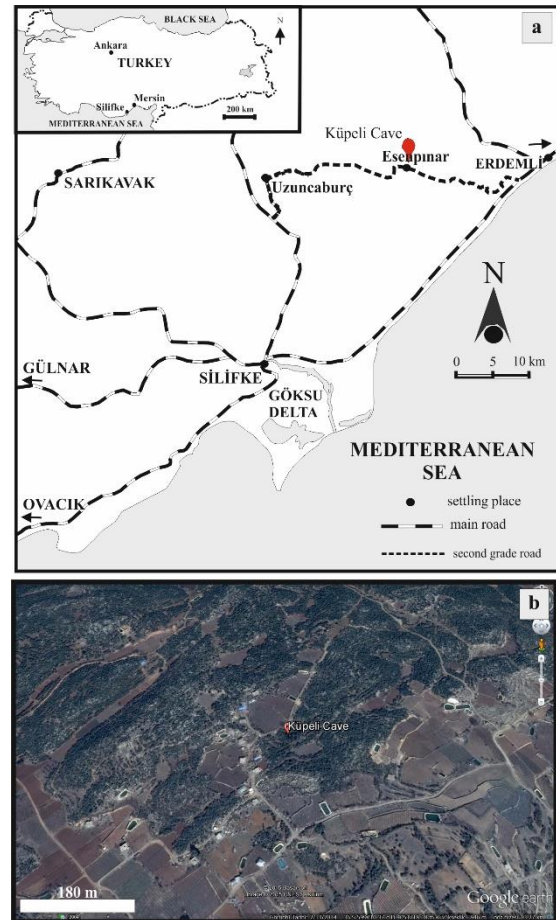


Figure 1. Location map (a) and satellite image (b) showing location of Küpeli Cave marked in red.

consistency with the distinctive tectonic lines which indicates the effect of tectonics on karstification. Karstification in the area, especially caves largely developed and shaped along NW-SE direction due to effects of discontinuities. The majority of the caves were developed at NW-SE direction (Akgöz, 2012; Akgöz and Eren, 2015).

### 2.3. Cave description

Küpeli Cave consists of two chambers which are connected with each other with a narrow passage (Figure 4). The first chamber is 30 m long, 20 m wide and 0.4 to 42 m in height. Entrance to the first chamber is provided by stairs from the collapsed portion of the roof (Figure 5 a). Whereas, the second chamber is of a smaller size being 17 m long, 9 m wide and 38 m in height. In the second room, speleothems are common. The first chamber is very poor in terms of cave deposits, however, several stalagmite development beneath dripping water was observed on the pile of broken parts below the collapsed portion of the cave ceiling (Figure 5 b-e).

## 3. MATERIALS AND METHODS

Only one calcium-rich water sample was taken by careful scraping with a sharp knife from upper surface of



Max – 2200 Ultia PC instrument with CuK $\alpha$  radiation and a scanning speed of 1°2 $\theta$  min<sup>-1</sup>. SEM-EDX analysis was performed using a JEOL JSM 5600LV instrument with an EDX detector. For SEM-EDX analysis, a piece of the precipitate was placed by adhering onto an aluminum sample holder with double-sides and coated with a film (~350 Å) of gold using a Giko ion coater. Differential thermal and thermogravimetry analyses (DTA-TG) (PerkinElmer – Pyris 1, USA) were obtained from the 10 mg of the powdered precipitated material in a Pt sample holder, heated at an average rate of 10°C/min with an alumina reference. IR spectroscopic analysis was carried out on the pressed powder sample with a size of less than 2  $\mu$ m mixed with KBr using a PerkinElmer 100 FT-IR spectrometer, and scan was run at 4 cm<sup>-1</sup> resolution.

The calcite precipitate was analysed for selected major and trace elements using both inductively coupled plasma-optical emission spectroscopy (ICP-OES) and inductively coupled plasma-mass spectroscopy (ICP-MS) methods in the Analytical Services Laboratory of the University of Greenwich (London, United Kingdom). This method was conducted after dissolution using a lithium metaborate fusion (Jarvis and Jarvis, 1992). In essence, 0.25 g of the sample was mixed with 1.25 g of lithium metaborate flux and fused at 900 °C. The molten bead was poured into weak nitric acid and stirred until dissolved. The resultant solution was made to volume. The analysis of major elements and some trace elements was undertaken using a Thermo ICAP 6500 ICP-OES with calibration via matrix-matched synthetic standards. Analysis of the remaining trace elements was completed using a Thermo X series 2 ICP-MS, again with calibration via matrix-matched synthetic standards and the use of CRMs and internal QC powders.

## 4. RESULTS

### 4.1. XRD determinations

The mineralogical composition of the precipitated material was determined by X-ray diffractometry. The results show that the precipitated material consists

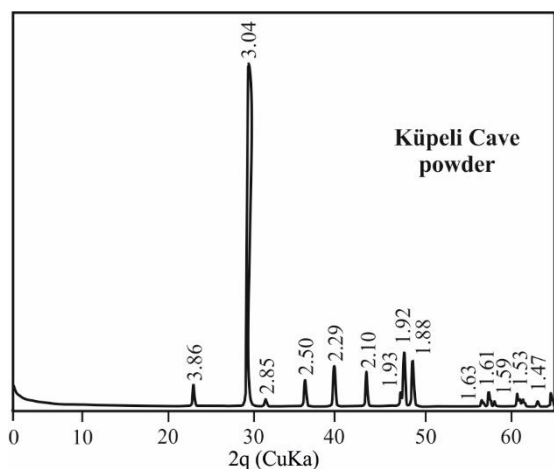


Figure 6. XRD patterns of newly formed calcite crystal from Küpeli cave.

entirely of calcite identified by peaks at 3.87, 3.04, 2.85, 2.50, 2.29, 2.10, 2.92, and 2.88 Å (Figure 6).

### 4.2. SEM-EDX analysis

SEM analyses were carried out on the precipitate that typically occurs as euhedral to subhedral equant calcite crystals with size of 5-10  $\mu$ m and filaments (Figure 7a-e). The filaments of the interwoven network have a length of approximately 10–20  $\mu$ m and a width up to 1  $\mu$ m, extending between the calcite crystals (Figure 7d-e). The EDX spectra of the crystals and filaments show strong peaks of Ca confirming the calcite composition (Figure 7f).

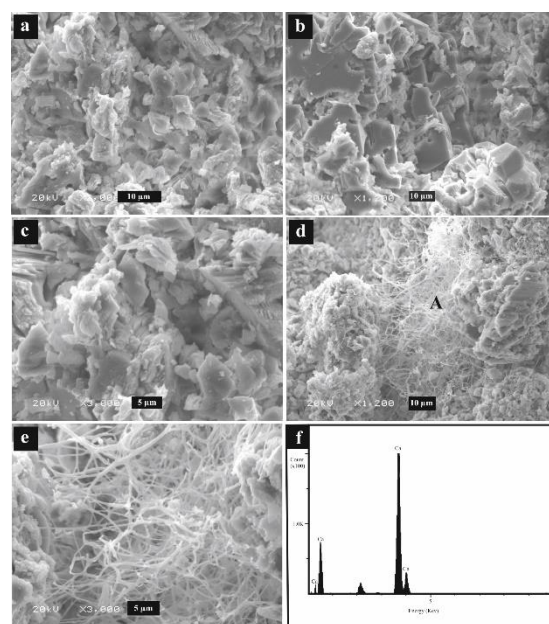


Figure 7. SEM images showing (a-c) newly formed calcite composed of euhedral and subhedral crystals; (d) filamentous green algae associated calcite crystals; (e) close view of (d); (f) EDX spectrum of newly formed calcite showing Ca peaks.

### 4.3. DTA-TG determinations

The DTA-TG curves of the calcite precipitate have a large endothermic peak at about 874°C (weight loss 46%) due to the decomposition of the calcite crystal structure (Figure 8). The result is consistent with those of stated by MacKenzie (1957), Webb and Krüger (1970) and Smykatz-Kloss (1974).

### 4.4. IR spectra

The IR spectra of the calcite sample is recognized by a diagnostic broad, intense band at 1417 cm<sup>-1</sup> and sharp bands at 874 and 712 cm<sup>-1</sup> corresponding to stretching vibration of the CO<sub>3</sub><sup>2-</sup> anions, out-of-plane bending mode, and in-plane bending vibrations, respectively (Figure 9; Van der Marel and Beutelspacher, 1976; Madejová et al., 2011).

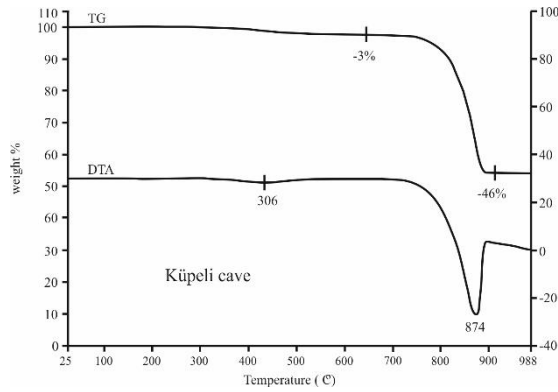


Figure 8. DTA-TG curves for newly formed calcite crystal from Kùpeli cave.

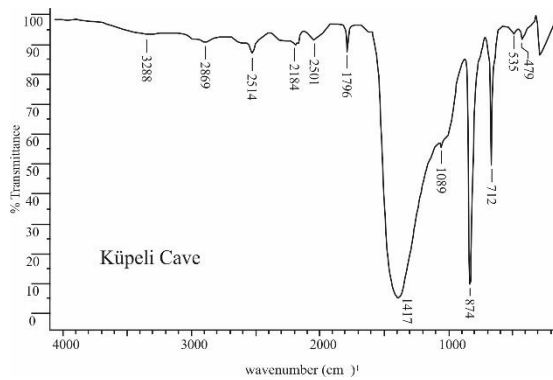


Figure 9. IR spectrum of newly formed calcite crystal from Kùpeli cave.

#### 4.5. Chemical Analysis

Chemical analysis of the precipitated material revealed that the precipitate is composed mainly of CaO (54.39 wt.%) and LOI (44.32 wt.%), and includes trace amount of SiO<sub>2</sub>, Al<sub>2</sub>O<sub>3</sub>, Fe<sub>2</sub>O<sub>3</sub>, TiO<sub>2</sub>, K<sub>2</sub>O, MgO, Na<sub>2</sub>O, P<sub>2</sub>O<sub>5</sub>, Mn, Ba, and Sr (Table 1). The chemical analysis are consistent with the results of XRD, SEM-EDX, DTA-TG and IR.

Table 1 Chemical composition of the precipitated calcite.

CaO	SiO <sub>2</sub>	Al <sub>2</sub> O <sub>3</sub>	Fe <sub>2</sub> O <sub>3</sub>	TiO <sub>2</sub>	K <sub>2</sub> O	MgO
wt.%	wt.%	wt.%	wt.%	wt.%	wt.%	wt.%
54.39	0.69	0.28	0.18	0.02	0.03	0.05

Na <sub>2</sub> O	P <sub>2</sub> O <sub>5</sub>	LOI	Total	Mn	Sr	Ba
wt.%	wt.%	wt.%	wt.%	mg/kg	mg/kg	mg/kg
0.01	0.07	44.32	100.04	16	70	7.4

#### 4.6 Stable isotope analysis

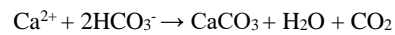
Stable isotope analysis was performed on the calcite precipitate. The results given in Table 2 indicate that  $\delta^{18}\text{O}$  and  $\delta^{13}\text{C}$  values of the calcite are  $-3.81$  and  $-6.92$  ‰ V-PDB, respectively.

Table 2. Stable isotope composition of the newly formed calcite.

$\delta^{18}\text{O}_{\text{V-PDB}}$ (‰)	$\delta^{13}\text{C}_{\text{V-PDB}}$ (‰)
$-3.81$	$-6.92$

## 5. DISCUSSION

Calcium carbonate is generally precipitated as calcite crystals in water supersaturated with respect to CaCO<sub>3</sub>. In this study, supersaturated water covering the upper surface of the stalagmites was scraped, then left to precipitate in a glass sample holder under the surface conditions including a surface temperature of 36 °C where evaporation increased concentration (activity) of Ca ions, and then caused precipitation of CaCO<sub>3</sub>. In the cave environment, precipitation conditions are probably provided during the dry seasons, and controlled by many factors such as temperature, water supply, humidity, and pCO<sub>2</sub> level (Day and Henderson, 2011). Calcium carbonate precipitation occurs by the reaction:



XRD and DTA-TG analyses revealed that the precipitated material is pure calcite showing all characteristic peaks. However, very low values of SiO<sub>2</sub>, Al<sub>2</sub>O<sub>3</sub>, K<sub>2</sub>O, MgO indicates presence of trace amount of impurities such as clay in the sample derived either from wind-blown dust or surface. Low Sr and Ba values are consistent with those of cave calcite (Sr 34–256 ppm and Ba < 40 ppm) (ongoing study in the same area; Verheyden et al., 2000; Fairchild et al., 2010; Wassenburg et al., 2012) and terrestrial (freshwater) sediments (Chen et al., 1997; Eren et al., 2008 for calcretes). Trace element contents in speleothems reflect water-rock and soil interaction time which is controlled by hydrological conditions and partitioning of the element from the water during calcite precipitation (Verheyden, 2004; Wassenburg et al., 2012; Vuai, 2012; Huang and Fairchild, 2001).

The  $\delta^{18}\text{O}$  and  $\delta^{13}\text{C}$  values of the precipitated calcite are  $-3.81$  ‰ V-PDB and  $-6.92$  ‰ V-PDB, respectively. The  $\delta^{18}\text{O}$  value indicates precipitation from meteoric water, and is higher than those (mean  $-5.38$  ‰ V-PDB) measured in speleothems (ongoing study in the Mersin area). Dominguez-Villar et al. (2008) and Day and Henderson (2011) reported mean  $\delta^{18}\text{O}$  values of  $-6.25$  and  $-6.82$  ‰ V-PDB for speleothems from Kaité Cave, northern Spain and for calcite grown under the cave-analogue conditions with drip rate of 1.6 drips/min, respectively. Similar  $\delta^{18}\text{O}$  values are reported by Riechelmann et al. (2013) as  $-5.6$  to  $-6.3$  ‰ V-PDB for watch glass calcite samples with different drip rate in the cave environment. The oxygen isotopic fractionation between water and carbonates is mainly temperature dependent (Poulson and White, 1969; Friedman and O'Neil, 1977; Talbot and Kelts, 1990; Lachniet, 2009; Deocampo, 2010). Since enrichment in the  $\delta^{18}\text{O}$  value of the precipitated calcite relative to those of the speleothem in the Mersin area and its counterparts in the literature is due to evaporation.

The  $\delta^{13}\text{C}$  value of the precipitated calcite is within the range of those of speleothems (ongoing study in the Mersin area; Bar-Matthews et al., 1997; McDermott, 2004) and also calcretes (Eren et al., 2008; Eren, 2011; Kaplan et al., 2013) indicating a contribution of light  $\text{CO}_2$  from the soil into percolating water due to reactions such as the root respiration and organic matter decomposition (Sherwin and Baldini, 2011).

Euhedral and subhedral calcite crystals in the SEM images with the  $\delta^{18}\text{O}$  and  $\delta^{13}\text{C}$  values indicate slow inorganic precipitation process from soil water by evaporation. However, presence of algal filaments in the SEM views may suggest another mechanism which is photosynthetic removal of  $\text{CO}_2$  (Cox et al., 1989). However, a network of algal filaments on the calcite crystals in local areas suggest that main mechanism is inorganic precipitation by which algal filaments were rapidly calcified at intense evaporation stage as final product of deposition (Jones and Kahle, 1993; Northup and Lavoie, 2001). In caves, loss of  $\text{CO}_2$  by diffusion from supersaturated solutions is the major cause of calcium carbonate precipitation (Cox et al., 1989). Under conditions where cave-air  $\text{PCO}_2$  is set at atmospheric levels, the supersaturation of fluid, and hence the growth depends mainly on the Ca content of water (Fairchild and McMillan, 2007) mainly controlled by evaporation rate. In the cave environment, evaporation is very slow compared to outside because of high moisture that causes massive macro-crystalline calcite in speleothem such as stalagmites (ongoing study; Bar-Matthews et al., 1997) that differs from crystal morphologies of the calcite precipitated from a thin cover of water under surface conditions.

## 6. CONCLUSION

Newly forming calcite precipitated from water supersaturated with respect to  $\text{CaCO}_3$  taken from a thin cover of water on the upper surface of stalagmites was analysed using a range of analytical techniques. XRD, IR, DTA-TG, and ICP-OES and ICP-MS analyses show that the precipitate consists almost entirely of calcite. SEM images revealed that the calcite precipitate mainly occurs as euhedral to subhedral equant crystals, and also includes green algal filaments extending between calcite crystals. The crystalline fabric and stable isotope values ( $\delta^{18}\text{O}$  and  $\delta^{13}\text{C}$ ) suggest slow inorganic precipitation from meteoric soil water. The algal filaments reflect rapid calcification at intense period of evaporation. Fabric difference between newly forming calcite and speleothems can be explained by environmental differences. In caves, calcite precipitation takes place under the high humidity and feedback or drip water mechanism whereas our sample characterizes precipitation under surface conditions where evaporation was dominant.

## REFERENCES

- Akgöz, M. (2012). Göksu nehri ve Lamas kanyonu (Mersin) arasında kalan bölgenin karst evrimi, PhD Thesis, Mersin University, Mersin, Turkey.
- Akgöz, M. and Eren, M. (2015). Traces of earthquakes in the caves: Sakarlık Ponor and Kepez Cave, Mersin (S Turkey). *Journal of Cave and Karst Studies*, Vol. 77, No. 1, 63–74.
- Baker, A. and Smart, P. L. (1995). Recent flowstone growth rates: Field measurements in comparison to theoretical predictions. *Chemical Geology*, Vol. 122, 121–128.
- Baker, A., Genty, D., Dreybrodt, W., Barnes, W. L., Mockler, N. J. and Grapes, J. (1998). Testing theoretically predicted stalagmite growth rate with Recent annually laminated samples: Implications for past stalagmite deposition. *Geochimica et Cosmochimica Acta*, Vol. 62, No. 3, 393–404.
- Bar-Matthews, M., Ayalon, A. and Kaufman, A. (1997). Late Quaternary Paleoclimate in the Eastern Mediterranean Region from Stable Isotope Analysis of Speleothems at Soreq Cave, Israel. *Quaternary Research*, Vol. 47, No. 2, 155–168.
- Baskaran, M. and Iliffe, T. M. (1993). Age determination of recent cave deposits using excess  $^{210}\text{Pb}$ - a new technique. *Geophysical Research Letter*, Vol. 20, No. 7, 603–606.
- Chen, Z., Chen, Z. and Zhang, W. (1997). Quaternary stratigraphy and trace-element indices of the Yangtze Delta, Eastern China, with special reference to marine transgressions. *Quaternary Research*, Vol. 47, No. 2, 181–191.
- Cox, G., James, J. M., Armstrong, R. A. L. and Leggett, K. E. A. (1989). Stromatolitic crayfish-like stalagmites. *Proceedings of the University of Bristol Speleological Society* 18, pp. 339–358.
- Day, C. C. and Henderson, G. M. (2011). Oxygen isotopes in calcite grown under cave-analogue conditions. *Geochimica et Cosmochimica Acta*, Vol. 75, No. 14, 3956–3972.
- Deocampo, D. M. (2010). Geochemistry of continental carbonates. In: Alonso-Zarza, A.M. and Tanner, L.H., Eds., *Carbonates in continental settings: geochemistry, diagenesis, and applications*. Amsterdam, Netherland, Elsevier, *Developments in Sedimentology* 62, pp. 1–59.
- Domínguez-Villar, D., Wang, X., Cheng, H., Martín-Chivelet, J. and Edwards, R. L. (2008). A high-resolution late Holocene speleothem record from Kaite Cave, northern Spain:  $\delta^{18}\text{O}$  variability and possible causes. *Quaternary International*, Vol. 187, No. 1, 40–51.
- Eren, M., 2008. Olba (Ura-Uğuralanı) jeoarkeolojisi (Silifke, Mersin). Ankara, Kültür ve Turizm Bakanlığı 24. Arkeometri Sonuçları Toplantısı, 181–192.
- Eren, M. (2011). Stable isotope geochemistry of Quaternary calcretes in the Mersin area, southern Turkey - A comparison and implications for their origin. *Chemie der Erde*, Vol. 71, No. 1, 31–37.

- Eren, M., Kadir, S., Hatipoğlu, Z. and Gül, M. (2008). Quaternary calcrete development in the Mersin area, southern Turkey. *Turkish Journal of Earth Sciences*, Vol. 17, No. 4, 763–784.
- Fairchild, I. J. and McMillan, E.A. (2007). Speleothems as indicators of wet and dry periods. *International Journal of Speleology*, Vol. 36, No. 2, 69-74.
- Fairchild, I. J. and Treble, P. C. (2009). Trace elements in speleothems as recorders of environmental change. *Quaternary Science Reviews*, Vol. 28, No. 5-6, 449–468.
- Fairchild, I. J., Spötl, C., Frisia, S., Borsato, A., Susini, J., Wynn, P. M., Cauzid, J. and EIMF (2010). Petrology and geochemistry of annually laminated stalagmites from an Alpin Cave (Obir, Austria): Seasonal cave physiology. *Geological Society, London, Special Publications* 336, 295–321.
- Friedman, I. and O'Neil, J. R. (1977). Compilation of stable isotope factors of geochemical interest. In: Fleischer, M., Ed., *Data of Geochemistry*. United States Geological Survey Professional Paper 440-KK, pp. 1–12.
- Gascoyne, M. and Nelson, D. E. (1983). Growth mechanisms of recent speleothems from Castleguard Cave, Columbia Icefields, Alberta, Canada, inferred from a comparison of uranium-series and carbon-14 age data. *Arctic and Alpine Research*, Vol. 15, No. 4, 537–542.
- Gedik, A., Birgili, Ş., Yılmaz, H. and Yoldaş, R. (1979). Mut-Ermenek-Silifke yöresinin jeolojisi ve petrol olanakları. *Türkiye Jeoloji Kurumu Bülteni*, Vol. 22, No.1, 7–26.
- Genty, D., Baker, A. and Vokal, B. (2001). Intra- and inter-annual growth rate of modern stalagmites. *Chemical Geology*, Vol. 176, No. 1-4, 191–212.
- Huang, Y. and Fairchild, I. J. (2001). Partitioning of  $\text{Sr}^{2+}$  and  $\text{Mg}^{2+}$  into calcite under karst-analogue experimental conditions. *Geochimica et Cosmochimica Acta*, Vol. 65, No. 1, 47–62.
- Jarvis, I. and Jarvis, K. E. (1992). Plasma spectrometry in earth sciences: techniques, applications and future trends. In: Jarvis, I. and Jarvis, K.E., Eds., *Plasma spectrometry in Earth Sciences*. *Chemical Geology* 95, pp. 1–33.
- Johnson, K. R., Hu, C., Belshaw, N. S. and Henderson, G. M. (2006). Seasonal trace-element and stable-isotope variations in a Chinese speleothem: The potential for high-resolution paleomonsoon reconstruction. *Earth and Planetary Science Letters*, Vol. 244, No. 1-2, 394–407.
- Jones, B. and Kahle, C. F. (1993). Morphology, relationship, and origin of fiber and dendritic calcite crystals. *Journal of Sedimentary Petrology*, Vol. 63, No. 6, 1018–1031.
- Kaplan, M. Y., Eren, M., Kadir, S. and Kapur, S. (2013). Mineralogical, geochemical and isotopic characteristics of Quaternary calcretes in the Adana region, southern Turkey: Implications on their origin. *Catena*, Vol.101, 164–177.
- Lachniet, M. S. (2009). Climatic and environmental controls on speleothem oxygen-isotope values. *Quaternary Science Reviews*, Vol. 28, No. 5-6, 412–432.
- Lauritzen, S. T. and Lundberg, J. (1999). Speleothems and climate: a special issue of *The Holocene*. *Holocene* Vol. 9, No. 6, 643–647.
- MacKenzie, R. C. (1957). *The Differential Thermal Investigation of Clays*. Mineralogical Society, London, UK.
- Madejová, J., Balan, E. and Petit, S. (2011). Application of vibrational spectroscopy to the characterization of phyllosilicates and other industrial minerals. *EMU Notes in Mineralogy*, Vol. 9, pp 171–226.
- McDermott, F. (2004). Palaeo-climate reconstruction from stable isotope variations in speleothems: a review. *Quaternary Science Reviews*, Vol. 23, No. 7-8, 901–918.
- Northup, D.E. and Lavoie, K.H., 2001. *Geomicrobiology of caves: a review*. *Geomicrobiology Journal*, Vol. 18, No. 3, 199–222.
- Poulson, T. L. and White, W. B. (1969). The cave environment. *Science*, Vol. 165, No. 3897, 971–981.
- Riechelmann, D. F. C., Deininger, M., Scholz, D., Riechelmann, S., Schröder-Ritzrau, A., Spötl, C., Richter, D. K., Mangini, A. and Immenhauser, A. (2013). Disequilibrium carbon and oxygen isotope fractionation in recent cave calcite: Comparison of cave precipitates and model data. *Geochimica et Cosmochimica Acta*, Vol. 103, 232–244.
- Sherwin, C. M. and Baldini, J. U. L. (2011). Cave air and hydrological controls on prior calcite precipitation and stalagmite growth rates: Implications for palaeoclimate reconstructions using speleothems. *Geochimica et Cosmochimica Acta*, Vol.75, No. 14, 3915–3929.
- Smykatz-Kloss, W., 1974. *Differential Thermal Analysis: Application and Results in Mineralogy*. Springer, Berlin.
- Talbot, M.R. and Kelts, K., 1990. Paleolimnological signatures from carbon and oxygen isotopic ratios in carbonates from organic carbonrich lacustrine sediments. In: Katz, B.J., Ed., *Lacustrine Basin Exploration: Case Studies and Modern Analogs*. Tulsa, Oklahoma, USA: American Association Petroleum Geologist Memoir 50, pp. 88–112.
- Tremaine, D.M., Froelich, P.N. and Wang, Y., 2011. Speleothem calcite farmed in situ: Modern calibration of  $\delta^{18}\text{O}$  and  $\delta^{13}\text{C}$  paleoclimate proxies in a continuously-

monitored natural cave system. *Geochimica et Cosmochimica Acta*, Vol. 75, No. 17, 4929–4950.

Turrero, M.J., Garrolon, A., Gomez, P., Martin-Chivelet, J., Sanchez, L. and Ortega, A.I., 2009. Present-day calcite deposition in two caves of N Spain (Kaite and Cueva Mayor): Factors affecting calcite growth and fabric. *Geochimica et Cosmochimica Acta*, Vol. 73, Supplement A1356.

Vaks, A., Bar-Matthews, M., Ayalon, A., Schilman, B., Gilmour, M., Hawkesworth, C.J., Frumkin, A., Kaufman, A. and Matthews, A., 2003. Paleoclimate reconstruction based on the timing of speleothem growth and oxygen and carbon isotope composition in a cave located in the rain shadow in Israel. *Quaternary Research*, Vol. 59, No. 2, 182–193.

Vaks, A., Bar-Matthews, M., Matthews, A., Ayalon, A. and Frumkin, A., 2010. Middle-Late Quaternary paleoclimate of northern margins of the Saharan-Arabian Desert: reconstruction from speleothems of Negev Desert, Israel. *Quaternary Science Reviews*, Vol. 29, No. 19-20, 2647–2662.

Van der Marel, H.W. and Beutelspacher, H., 1976. *Atlas of Infrared Spectroscopy of Clay Minerals and Their Admixtures*. Amsterdam, Netherland:Elsevier.

Verheyden, S., 2004. Trace elements in speleothems- A short review of the state of art. *International Journal of Speleology*, Vol. 33, No 1/4, 95–101.

Verheyden, S., Keppens, E., Fairchild, I.J., McDermott, F. and Weis, D., 2000. Mg, Sr and Sr isotope geochemistry of a Belgian Holocene speleothem: implications for paleoclimate reconstructions. *Chemical Geology*, Vol. 169, No. 1-2, 131–144.

Verheyden, S., Nader, F.H., Cheng, H.J., Edwards, L.A. and Swennen, R., 2008. Paleoclimate reconstruction in the Levant region from the geochemistry of a Holocene stalagmite from the Jeita cave, Lebanon. *Quaternary Research*, vol. 70, No. 3, 368-381.

Vuai, S.A.H., 2012. *Geochemical Characteristics of Spaleotherm Formation in Caves from Zanzibar Island, Tanzania*. 1:505. doi:10.4172/scientificreports.505.

Wassenburg, J.A., Immenhauser, A., Richter, D.K., Jochum, K.P., Fietzke, J., Deininger, M., Goos, M., Scholz, D. and Sabaoui, A., 2012. Climate and cave control on Pleistocene/Holocene calcite-to-aragonite transitions in speleothems from Morocco: Elemental and isotopic evidence. *Geochimica et Cosmochimica Acta*, Vol. 92, 23–47.

Webb, T.L. and Krüger, J.E., 1970. Carbonates. In: MacKenzie, R.C., Ed., *Differential Thermal Analysis Vol. 1 - Fundamental Aspects*. Academic Press, London.

Copyright © Turkish Journal of Engineering (TUJE). All rights reserved, including the making of copies unless permission is obtained from the copyright proprietors.

# Turkish Journal of Engineering



*Turkish Journal of Engineering (TUJE)*  
*Vol. 1, Issue 2, pp. 52-60, September 2017*  
*ISSN 2587-1366, Turkey*  
*DOI: 10.31127/tuje.316220*  
*Research Article*

## **REGRESSION MODELING OF THE HOLE QUALITIES DURING COLD WORK TOOL STEELS DRILLING, WITH DIFFERENT CHARACTERISTICS DRILL BITS**

İskender Özkul <sup>\*1</sup>, Berat Barış Buldum <sup>2</sup> and Adnan Akkurt <sup>3</sup>

<sup>1</sup>Mersin University, Engineering Faculty, Department of Mechanical Engineering, Mersin, Turkey  
(iskender@mersin.edu.tr)

<sup>2</sup>Mersin University, Engineering Faculty, Department of Mechanical Engineering, Mersin, Turkey  
(barisbuldum@mersin.edu.tr)

<sup>3</sup>Gazi University, Technology Faculty, Department of Industrial Design Engineering, Ankara, Turkey  
(aakkurt@gazi.edu.tr)

---

\* Corresponding Author

Received: 12/04/2017

Accepted: 18/05/2017

---

**ABSTRACT** In this study, drill operations have been tested on Sleiþner cold work tool steel by various machining parameters and drill bits. Solid Carbide Uncoated drill bits and TiAlN Coated reamed drill bits were used in experiments. Both drill bits were machined on Sleiþner steel with four different cutting speeds. After machining, thrust forces and moments values generated during cutting, consisting surface and the hole qualities have been measured. Drilled by reamed drill bit's hole gave better results quality as a result of the studies. It was reached as conclusion that the optimum values parameters of the cutting speeds are between 40 to 42 m/min for both the drill bits.

**Keywords:** *Machinability, Drilling cutting forces, Surface roughness, cold work tool steel*

## 1. INTRODUCTION

As a result of further customization of industrial manufacturing types, special alloy steels are now being used more frequently. The use of alloyed steels has increased, leading to much more successful results than conventional steel. Tool steels are more valuable than standard steels because they are specially produced and produced according to the work type. In order to use these steels in the most efficient way, the manufacturing steel processing parameters in general quality need to be updated to the level of qualified tool steel. That's why it's so important to choose the right steel for the job, as well as having knowledge of how to machining it. Slepner from cold work tool steel grades are commonly used as sheet forming molds in places where wear is observed ([www.uddeholm.com](http://www.uddeholm.com)). This steel is also used in industry for sheet metal forming where generally in sheet metal cutting and tearing applications up to 3 mm in high-durability materials requiring low maintenance, in cuts of hard and thin sheets (such as lamination molds), and in iron and steel plants. It is used in places where high abrasion resistance is required, high toughness, high compression strength, good tempering resistance and compatibility with surface treatment

At the same time, that alloy is suitable for surface coating techniques like nitration, Tin and CrN coated by PVD. As well as it can be used in plastic molds, hard and additive plastics and injection molds which are expected to have very high molding life ([www.uddeholm.com](http://www.uddeholm.com)). Material shaping technique is as important as material selection. Achieving the desired quality at the lowest time and costs is one of the factors affecting the productivity of the work. Material shaping is often encountered in the form of holes.

Though drilling can be achieved in many different ways in manufacturing technology, drilling is the most popular method in machining, which is the conventional machining method. This method gradually renews itself in the fields of material, coating and tool geometry technology. Technological advances in providing tool components usually focuses increasing the surface processing speed and precession on the correction quality.

When the studies done in the literature are examined; Ohzeki et al. (Ohzeki, Hoshi et al. 2012) predicted that the shear forces generated during drilling on the carbon fiber reinforced plastic composite are related to delamination during drilling. They have developed a machining system that changes the cutting forces which vary with the predetermined feedrate according to the axial shear force values obtained by the piezoelectric dynamometer. The performance of the developed system has been confirmed by test running.

In addition, the drilling tests were carried out by considering the possibility of drilling errors in the CFRP composites with cutting force feedback. No significant deformation has been observed in the tests made by taking feedback under specific conditions. Tash et al. (Tash, Samuel et al. 2012) have studied the machining and computation of force and moment which result from the machinability of 356 and 319 aluminum alloys subjected to heat treatment. As a result of the experiments, a long tool life was obtained at the processing of low Mg-content 319 alloys (0,1%). Salimi et al. (Salimi, Abbasgholizadeh et al. 2011), used artificial neural networks to study the abrasions that occurred on the drill

during drilling. They reported that the results of the experimental studies and artificial neural network models were very similar. Farid et al. (Farid, Sharif et al. 2011) examined chip morphology for high-speed drilling of Al-Si alloys. They observed that cutting parameters were a major influence on chip morphology. Zitoune and et al. (Zitoune, Krishnaraj et al. 2012) examined the performance of a nano-plated drill on carbon fiber reinforced plastic / aluminum sandwiches.

As a result of the experiments, it is seen that the progression rate is a significant influence on the formation of the chip size and pattern. They found that the axial cutting forces on the composite plate were less than 10-15% of that of the uncoated drill and about 50% on the aluminum.

When examining both drills, it has been found that the nano-plated drills are considerably successful in terms of surface roughness and axial forces. Çiçek and Kivak et al. (Çiçek, Kivak et al. 2012) studied the performance of cryonically machined M35 HSS drills on austenitic stainless steels. The machined exposed cutting tool shows better results in terms of axial forces, surface roughness, tool life and wear at 304 and 316 stainless steel at different cutting and feed speeds compared to the non-machined insert.

As a result of the tests it was understood that it is more difficult to process 304 stainless steel to 316 stainless steel. İsbilir and Ghassemieh (İsbilir and Ghassemieh 2012) have worked on the analysis of carbon fiber reinforced composite drilling by the finite element method. In the study, the experimental results were modeled with 3D finite element and the results were compared.

Our study has been carried out on Slepner cold work tool steel by a new product a self-reamed TiAlN coated carbide drill and uncoated carbide drill. End of the experiments, the cutting forces, surface roughness, dimensional accuracy and deviation from circularity obtained and the results were investigated.

## 2. EXPERIMENTAL

### 2.1 Material and Method

The chemical composition of the cold work tool steel Slepner alloy used in the experimental work is given in Table 1.

The Slepner steel industry has been chosen for its multi-purpose use, which is often used in metal sheet forming and construction such as long-life plastic injection molds. The materials used in the work are cut by sawing in the dimensions given in Fig. 1 and then the surface is machined in the CNC vertical machining to ensure surface cleanliness and parallelism. Pre-drilling is not carried out before drilling in CNC vertical machining.

Table 1. Chemical composition of Slepner cold work tool steel (Özkul 2012)

C	Mn	Cr	Mo	V
0,90	0,5	7,8	2,5	0,5

Slepner cold work tool steel delivery is 235 HB. Physical properties of the product are shown in Table 2.

Table 2. Slepner cold work tool steel physical properties (www.uddeholm.com)

Temperature °C	20	200	400
Density (g/cm <sup>3</sup> )	7,73	7,68	7,60
Thermal Expansion Coefficient	-	11,6*10 <sup>-6</sup>	12,4*10 <sup>-6</sup>
Thermal conductivity (W/M°C)	-	20	25
Modulus of Elasticity (MPa)	205000	190000	180000
Specific Heat (j/Kg °C)	460	-	-

The test specimens are shown in Figure 1 prepared in dimensions of 24x60x240mm.

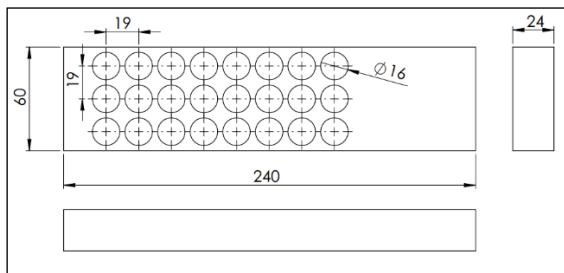


Fig. 1. Test sample (Özkul 2012)

Fig. 2 shows the workpiece and the holes through which the dynamometer is mounted.

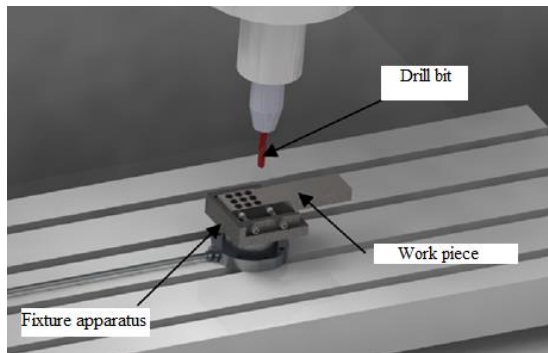


Fig. 2. Fixture apparatus

Two different types of carbide drills with a diameter of 16 mm were used in the holes to be made by vertical machining in the CNC machine. The forms of the self-tapping carbide drill and the carbide drill as tool geometries are shown in Fig. 3.

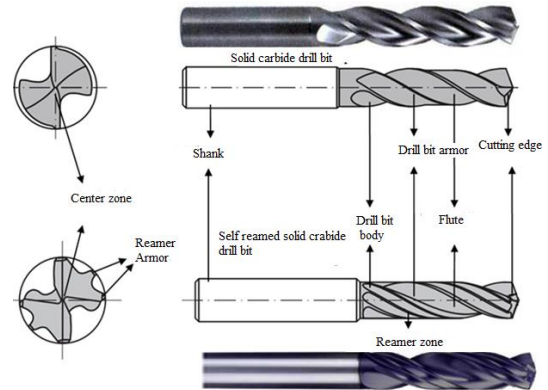


Fig. 3. Tool geometry of carbide drills (Özkul 2012)

The tool has an end angle ( $\Psi$ ) of 140° and a helix angle ( $\gamma$ ) of 30°. Coating of self-encrusted carbide drill is TiAlN (Titanium Aluminium nitride) and the other carbide drill is uncoated.

## 2. Drilling Operations

Vertical machining experiments were carried out at the Johnford VMC-550 CNC vertical machining centre. The technical characteristics of vertical processing are given in Table 3.

Table 3. Technical specifications of the vertical machining centre used in the experiments

Power	5,5 kW
Max. rpm	8000 rpm
x, y, z axis length	600, 500, 600 mm
Precession	0,001 mm
Operating system	Fanuc

The cutting parameters used for both cutting tools are given in Table 4 below. Cooling fluid was used during drilling.

Table 4. Cutting parameters used in experiments

Feed rate (mm/rpm)	Cutting speed (m/min)
0,16	36-40-44-48

Experiments were carried out at 4 different cutting speeds. The applied cutting speed parameters are 3 holes processed on the sample with the same cutting tool. The mean values of the data generated during the machining and the surface are used in the graphs. The thrust forces and moment values generated during the cutting process are measured with a dynamometer. In the experiment, quantities of deviation and circularity of the hole geometry were determined by the coordinate measuring machine CMM (Coordinate Measuring Machine) on the holes and surfaces formed after the machining operation was finished. The roughness amounts of the holes formed on the surface of the hole are measured by the surface roughness device, the measured parameters are given in Table 5 below.

Table 5. Cutting parameters used in experiments (Özkul 2012)

Experiment Code	Feed rate (mm/rpm)	Cutting speed (m/min)	Thrust force (N)	Moment (Ncm)	Diameter Deviation (mm)	Circularity Deviation (mm)	Average Surface Roughness ( $\mu\text{m}$ )
RM-1-1	0,16	36	2641	1720	0,008	0,044	1,315
RM-1-2		36	2734	2120	0,003	0,034	1,264
RM-1-3		36	2874	2175	0,01	0,045	0,957
RM-2-1		40	2537	1646	0,009	0,009	1,11
RM-2-2		40	2518	1722	0,011	0,045	1,003
RM-2-3		40	2531	1814	0,007	0,012	1,271
RM-3-1		44	2519	1622	0,022	0,022	0,923
RM-3-2		44	2517	1702	0,017	0,008	0,674
RM-3-3		44	2537	1777	0,021	0,002	1,023
RM-4-1		48	2517	1648	0,021	0,009	0,836
RM-4-2		48	2521	1657	0,021	0,011	0,785
RM-4-3		48	2486	1669	0,024	0,004	0,815
KM-1-1	0,16	36	3775	2121	0,006	0,095	2,771
KM-1-2		36	3978	1856	0,003	0,021	0,948
KM-1-3		36	3861	1651	0,008	0,012	1,555
KM-2-1		40	3830	1797	0,007	0,022	2,621
KM-2-2		40	3685	1754	0,004	0,012	0,886
KM-2-3		40	3866	1650	0,007	0,021	1,629
KM-3-1		44	3950	1745	0,01	0,025	2,735
KM-3-2		44	3607	1658	0,008	0,012	0,995
KM-3-3		44	3301	1735	0,014	0,013	1,327
KM-4-1		48	3598	1718	0,015	0,014	1,482
KM-4-2		48	3441	1695	0,018	0,009	1,681
KM-4-3		48	3685	1689	0,009	0,016	1,697

RM : Self-reamed TiAlN Coated drill bit  
KM : Uncoated carbide drill bit

### 3. EXPERIMENTAL AND STATISTICAL ANALYSIS RESULTS AND DISCUSSION

#### 3.1. Experiment and Statistical Analysis

The parameters of different cutting speeds used in the experiments have been determined the thrust force, moment, surface roughness, deviation and deviation from the circularity on the specimens of the different types of drills. The data were analysed by ANOVA (analysis of variance / variance analysis) and different methods using MS Excel software. The values used in the works are the average of the values of the same 3 holes processed with the same parameters in Table 5.

Estimated values are shown in the graphs, depending on the data obtained from the experiments performed and the statistical predicted values and the 10% increase in the independent variables in the 3 levels not used in the experiments. The values used are as dummy model, with self-reamed drill bit dedicated as "1" and carbide drill bit dedicated as "0" value. The obtained regression equations are valid for the values for which the cutting speed is not "0" value.

#### 3.2. Analysis of Thrust Force

The model summary of the thrust force with the values obtained as the results of the experiments is given in the ANOVA analysis, Table 6 and Table 7.

$R^2$ , the number of determinants of the model, represents the rate of the independent variable, cutting rate, and the relation of the drill type to the dependent variables. The  $R^2$  value of 0,993 indicates that the percentage of the association is around 99,3%. This value is very close to 100 percent, indicating how the bond is strong structure.

$R^2$ , the number of determinants of the model, represents the rate of the independent variable, cutting rate, and the relation of the drill type to the dependent variables. The  $R^2$  value of 0,993 indicates that the percentage of the association is around 99,3%. This value is very close to 100 percent, indicating how the bond is strong structure.

Table 6. Thrust force model

Regression Statistics	
Multi R	0,997
$R^2$	0,993
arranged $R^2$	0,990
Standard Error	61,198
Observation	8

Table 7. ANOVA table for thrust force

ANOVA					
	<i>SD</i>	<i>KT</i>	<i>KO</i>	<i>F</i>	<i>significance F</i>
Regression	2	2666348	1333174	356	0,000
Difference	5	18726	3745		
Total	7	2685074			

	<i>coefficients</i>	<i>Standard Error</i>	<i>t Stat</i>	<i>P-value</i>
Intersection	4656	205,49	22,66	0,00
Drill type ( <i>Mt</i> )	-1137	43,27	-26,28	0,00
Cutting rate ( <i>Vc</i> )	-22	4,84	-4,63	0,01

When the significance coefficient of ANOVA output is less than 0,000 in 0,05, regression models are evaluated as significant. The linear regression equations for the thrust force (*Cf*) of the system are given in Eq (1).

$$Cf = 4656 - 1137Mt - 22Vc \quad (1)$$

Fig. 4 shows the predicted values of the thrust force and the different regression models of the cutting rate parameters, which are not experimentally realized but are increased by 10%.

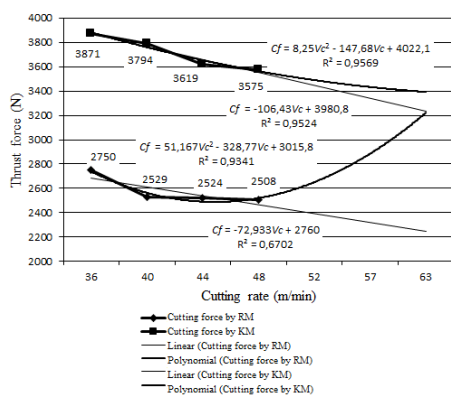


Fig. 4. Thrust force value change graph against increasing untested test parameters at 10%

As seen in Fig. 4, in the RM drill, less force is observed at increasing cutting speeds than in the MM drill. Although there is no about 0,1% force difference between 40 m / min and 44 m / min in the RM drill, the increase in the KM drill at the same cutting speed values is around 1,04%.

When the  $R^2$  values are examined, it is seen that only the value of the self-taught drill has a value of 67,02% in the linear regression, while the others show very successful results.

Table 8. Moment values model

Regression Statistics	
Multi R	0,833
$R^2$	0,694
Arranged $R^2$	0,571
Standard Error	76,219
Observation	8

The  $R^2$  value of the resulting model was 0,694 (69,4%). The resulting value does not seem very strong.

Table 10. ANOVA table for moment values

ANOVA					
	<i>SD</i>	<i>KT</i>	<i>KO</i>	<i>F</i>	<i>Significance F</i>
Regression	2	65778,0	32889,0	5,7	0,052
Difference	5	29046,9	5809,4		
Total	7	94824,9			

	<i>Coefficients</i>	<i>Standard errors</i>	<i>t Stat</i>	<i>P-values</i>
Intersection	2603,6	255,9	10,2	0,000
Drill type ( <i>Mt</i> )	16,9	53,9	0,3	0,766
Cutting rate ( <i>Vc</i> )	-20,2	6,0	-3,4	0,020

Since the significance coefficient of ANOVA output is too small at 0,05 than 0,05, the regression models are meaningless. The linear regression equations for the system's moment value (*Mo*) are given in Eq (2).

$$Mo = 2603,6 - 16,9Mt - 20,2Vc \quad (2)$$

Fig. 5 shows the predicted values of the torque values with different regression models and the torque values increased by 10%, which is not carried out as an experiment.

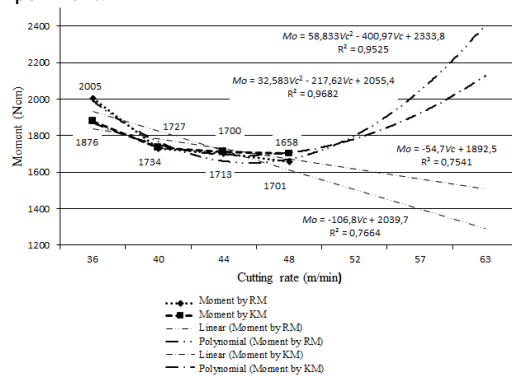


Fig. 5. Moment value change graph against increasing untested test parameters at 10%

In Fig. 5, there is a difference of less than 1% on average at speeds of 40-44-48 m / min. However, in the

test results at a cutting speed of 36 m / min, a difference of about 6% between the drills can be explained as the RM drill has exposed the reamer's armor to the extra surface. Table 11 contains the  $R^2$  values and equations that occur in Fig. 5.

When the  $R^2$ 's are examined, interpreting the polynomial regression estimates is more successful because the linear regression values of the self-aligning drill and the uncoated carbide drill are lower than the polynomial values.

### 3.4. Analysis of surface quality

The model summarized using the obtained average surface roughness values is given in ANOVA analysis, Table 10 and Table 11.

Table 10. Average surface roughness model

<i>Regression Statistics</i>	
Multi R	0,986
$R^2$	0,973
Arranged $R^2$	0,962
Standard error	0,076
Observation	8

Since the value of  $R^2$  of the resulting model is 0,973 and 97,3%, it is very strong.

Table 11. ANOVA table for average surface roughness values

ANOVA					
	<i>SD</i>	<i>KT</i>	<i>KO</i>	<i>F</i>	<i>Significance F</i>
Regression	2	1,049	0,525	90,155	0,000
Differences	5	0,029	0,006		
Total	7	1,078			

	<i>Coefficients</i>	<i>Standard errors</i>	<i>t Stat</i>	<i>P-values</i>
Intersections	2,636	0,256	10,293	0,000
Drill type ( <i>Mt</i> )	-0,696	0,054	-12,902	0,000
Cutting rate ( <i>Vc</i> )	-0,022	0,006	-3,721	0,014

The regression models are significant because the significance coefficient in the ANOVA output is less than 0,05 in 0,05. The linear regression equations for the surface roughness values ( $Y_p$ ) of the system are given in Equation 3.

$$Y_p = 2,636 - 0,696Mt - 0,022Vc \quad (3)$$

Fig. 6 shows the predicted values of different regression models and average surface roughness values of the cut-off speed parameters, which are increased by 10%, which are not carried out as experiments.

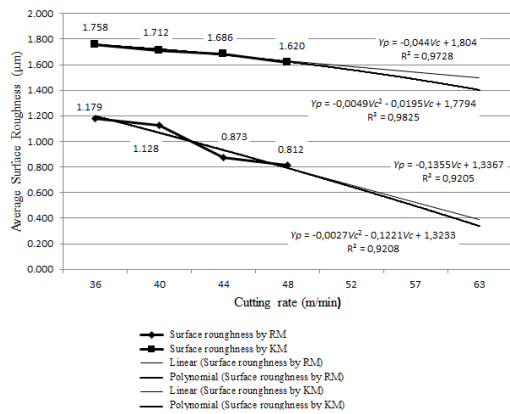


Fig. 6. Average surface roughness value change graph against increasing untested test parameters at 10%

Table 13. ANOVA table for dimension deviation

ANOVA	<i>SD</i>	<i>KT</i>	<i>KO</i>	<i>F</i>	<i>Significance F</i>
Regression	2	0,000	0,000	16,190	0,007
Difference	5	0,000	0,000		
Total	7	0,000			

	<i>Coefficients</i>	<i>Standard error</i>	<i>t Stat</i>	<i>P-values</i>
Intersection	-0,036	0,009	-3,909	0,011
<i>Drill type (Mt)</i>	0,005	0,002	2,801	0,038
<i>Cutting rate(Vc)</i>	0,001	0,000	4,953	0,004

Since the value of  $R^2$  of the resulting model is 86,6%, the value appears strong.

The regression models are significant because the significance coefficient of ANOVA outputs is less than 0,07. The linear regression equations for the system deviation (EQ) are given in Eq. (4).

$$\zeta_s = -0,036 + 0,005Mt + 0,001Vc \quad (4)$$

Fig. 7 shows the predicted values of the cut-off speed parameters, which are not realized in the experiment but increased depending on the 10% increase, with different regression models.

In figure 6, the value obtained by the RM drill at a cutting speed of 48 m / min produced a smoother surface than the other cutting speeds. The improvement from 48 m / min to 44 m / min in the RM drill is about 7%. However, at a cutting speed of 48 m / min, less smoothness was obtained with a value of about 4% compared to the speed of 44 m / min in the PM drill. Compared to the best values of the two cutting tools, it is observed that the RM drill has a clearly better surface. This difference can be considered as beneficial to the reamer armor and its coating that the RM drill is different from the MM drill. When the  $R^2$ 's were examined, it was observed that the obtained values were quite good but in general polynomial values were more successful.

### 3.5. Diameter Deviation Analysis

The model summarized using the obtained deviation values is given in ANOVA, Table 12 and Table 13.

Table 12. Diameter Deviation model

<i>Regression Statistics</i>	
Multi R	0,931
$R^2$	0,866
Adjusted $R^2$	0,813
Standard error	0,003
Observation	8

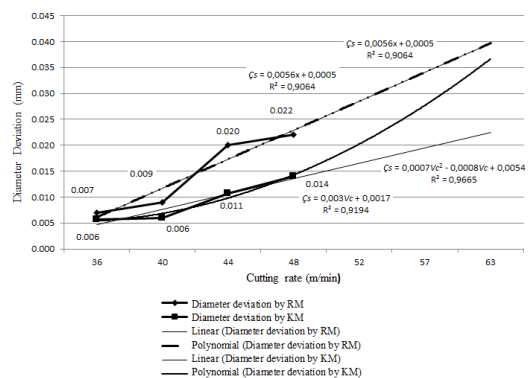


Fig. 7. Diameter dimension value change graph against increasing untested test parameters at 10%

In product processing, reaching the finished product and performing the operation within acceptable geometric tolerance while performing this operation is the biggest goal of the manufacturer. At this point, job efficiency will be increased, and unwanted expenses and losses will be avoided. This is why it is necessary to determine the quality of the work and to investigate and use the possibilities to save time. When the values in the graphs in Figure 7 are examined, it is seen that the deviation values decrease with decreasing cutting speed in general. Although there is no significant difference between the drill bit graphs of 36 and 40 m/min in both drill graphs, there is an increase of about 222% in the RM drill at the speed of 44 m / min and about 83% at the drill bit. The cutting speed of 36 m / min was determined as the speed at which extreme deviations occurred in both drills. When  $R^2$  were examined, linear and polynomial regression values for RM drill values were found to be the same. It was observed that the linear regression gave a more positive result for the KM mathematics than the obtained results.

Table 15. ANOVA table of Deviation from Circularity

ANOVA					
	<i>SD</i>	<i>KT</i>	<i>KO</i>	<i>F</i>	<i>Significance F</i>
Regression	2	0,001	0,001	11,939	0,012
Difference	5	0,000	0,000		
Total	7	0,001			

	<i>Coefficients</i>	<i>Standard error</i>	<i>t Stat</i>	<i>P-value</i>
Intersection	0,128	0,022	5,841	0,002
<i>Drill type(Mt)</i>	-0,002	0,005	-0,487	0,647
<i>Cutting rate (Vc)</i>	-0,003	0,001	-4,862	0,005

The regression models are meaningful because the significance coefficient of ANOVA outputs is less than 0,05 as 0,012. The linear regression equations for the system deviation ( $D_s$ ) are given in Eq. (5).

$$D_s = 0,128 - 0,002Mt - 0,003Vc \quad (5)$$

Fig. 8 shows the predicted values of the various regression models and deviation from the circularity of the cut-off speed parameters, which are increased by 10%, which are not performed as experiments.

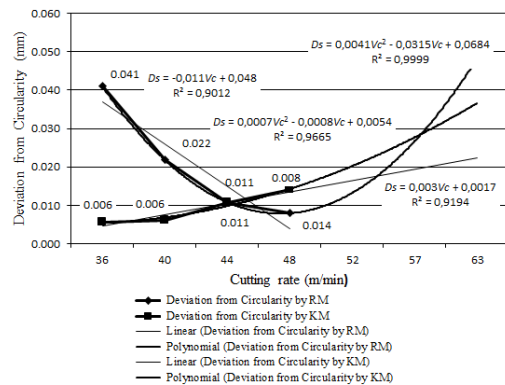


Fig. 8. Deviation from circularity value change graph against increasing untested test parameters at 10%

### 3.6. Deviation from Circularity

The model summarized using the deviation values obtained from the obtained circularity is given in ANOVA analysis, Table 14 and Table 15. Table 14. Deviation from Circularity model

<i>Regression Statistics</i>	
Multi R	0,909
$R^2$	0,827
Arranged $R^2$	0,758
Standard error	0,007
Observation	8

The resulting value is strong due to the fact that the  $R^2$  value of the resulting model is 82,7%.

When checking the graphs in Figure 8, it is clear that, in general, there is no significant change in the PM drill at 40-44 m/min of deviation from the circularity, but there is more change in the RM drill at the same speed. The cutting speed of 36 m/min was found to be the least ideal of the values applied in both drills, so that the deviations from the drill were small. When  $R^2$  was examined, it was found that the polynomial regression values were better than linear values, and the 99,99% value obtained for RM drill shows that there is a correlation between them.

### 4. CONCLUSION

The results obtained in the light of the values obtained by removing the chips by drilling with different quality cutters on the cold work tool steel are summarized below.

- The force and torques generated during cutting on the Sleiپner cold work tool steel are seen in the moment diagram of the RM drill, which cuts more easily than the KM drill. However, RM is forced to cut at low cutting speed because the reamer armor forced to cut for RM drill.
- A difference of about 93% was observed in the surface roughness of the RM drill at a speed of 44 m / min compared to the KM drill bit. The reamer armor on this side showed its quality in this work. If sensitivity is

- required on the desired surface, the RM drill is better in terms of machining time because it makes two operations together.
- In the deviation tolerance values of the dimension, it is seen that at low cutting speed, RM drill has very similar values like 15% with KM drill. The KM drill bit that the dimension deviations performance was better, while at cutting speed of 44 m/min of the RM drill, the KM matched the positive result with a difference of 54%.
  - Even though the self-reamed drill bit is costlier than the other drill, it is more suitable than the uncoated carbide drill bit with the surface quality and the amount of time it is saved and the amount of workmanship.

#### ACKNOWLEDGEMENTS

We would like to thank ASSAB KORKMAZ Çelik ve Isıl İşlem AŞ for their support.

#### REFERENCES

- Çiçek, A., T. Kıvık, I. Uygur, E. Ekici and Y. Turgut (2012). "Performance of cryogenically treated M35 HSS drills in drilling of austenitic stainless steels." *The International Journal of Advanced Manufacturing Technology* Vol. 60, No. 1 pp. 65-73.
- Farid, A. A., S. Sharif and M. H. Idris (2011). "Chip morphology study in high speed drilling of Al-Si alloy." *The International Journal of Advanced Manufacturing Technology* Vol. 57, No. 5-8 pp. 555-564.
- İsbilir, O. and E. Ghassemieh (2012). "Finite element analysis of drilling of carbon fibre reinforced composites." *Applied Composite Materials* Vol. 19, No. 3-4 pp. 637-656.
- Ohzeki, H., H. Hoshi and A. Fumihito (2012). "Drilling of carbon fiber reinforced plastic composites with feedback control based on cutting force." *Journal of Advanced Mechanical Design, Systems, and Manufacturing* Vol. 6, No. 1 pp. 52-64.
- Özkul, İ. (2012). Takım çeliği malzemelerin geleneksel ve modern işleme yöntemleri ile işlenebilirliklerinin araştırılması Master thesis, Gazi University, Ankara, Turkey.
- Salimi, A., S. Abbasgholizadeh, S. Taghizadeh and A. Safarian (2011). "Using of artificial neural Networks to predict drill wear in machining process." *Australian Journal of Basic and Applied Sciences* Vol. 5, No. 12 pp. 2752-2760.
- Tash, M. M., F. Samuel and S. Alkahtani (2012). "Machinability of Heat-Treated 356 and 319 Aluminum Alloys: Methodology for Data Processing and Calculation of Drilling Force and Moment." *Advanced Materials Research* Vol. 396, No. pp. 1008-1022.
- [http://www.uddeholm.com/files/PB\\_Uddeholm\\_sleipner\\_english.pdf](http://www.uddeholm.com/files/PB_Uddeholm_sleipner_english.pdf). [Accessed 26 May 2017].

Zitoune, R., V. Krishnaraj, B. S. Almabouacif, F. Collombet, M. Sima and A. Jolin (2012). "Influence of machining parameters and new nano-coated tool on drilling performance of CFRP/Aluminium sandwich." *Composites Part B: Engineering* Vol. 43, No. 3 pp. 1480-1488.

Copyright © Turkish Journal of Engineering (TUJE). All rights reserved, including the making of copies unless permission is obtained from the copyright proprietors.

# Turkish Journal of Engineering



*Turkish Journal of Engineering (TUJE)*  
*Vol. 1, Issue 2, pp. 61-65, September 2017*  
*ISSN 2587-1366, Turkey*  
*DOI: 10.31127/tuje.317778*  
*Research Article*

## **THE INVESTIGATION ON ELECTRICAL AND OPTICAL PROPERTIES OF CdO/CNT NANOCOMPOSITE**

Ömer Guler <sup>\*1</sup>, M. Gökhan Albayrak <sup>2</sup>, Mehmet Takgün <sup>3</sup> and Seval Hale Güler <sup>4</sup>

<sup>1</sup>Mersin University, Engineering Faculty, Department of Metallurgical and Materials Engineering, Mersin, Turkey  
(oguler@mersin.edu.tr) (shguler@mersin.edu.tr)

<sup>2</sup>Firat University, Engineering Faculty, Department of Metallurgical and Materials Engineering, Elazığ, Turkey  
(mgalbayrak@firat.edu.tr)

<sup>3</sup>Firat University, Engineering Faculty, Department of Metallurgical and Materials Engineering, Elazığ, Turkey  
(mehmet\_takgun@hotmail.com)

<sup>4</sup>Mersin University, Engineering Faculty, Department of Metallurgical and Materials Engineering, Mersin, Turkey  
(shguler@mersin.edu.tr)

---

\* Corresponding Author

Received: 15/04/2017      Accepted: 19/05/2017

---

### **ABSTRACT**

In this study, composite materials reinforced with carbon nanotubes (CNT) containing cadmium oxide were produced and investigated optical and electrical properties of them. Carbon nanotubes which used support materials were synthesized by chemical vapor deposition. After then, they were reinforced in to the cadmium oxides which were sold by commercial. As another group, cadmium oxides were synthesized by sol-gel method and reinforced carbon nanotubes with different rate. Synthesized CNT's were subjected to TEM investigation. Obtained CNT's were also subjected to SEM as structural. After those, gained composite samples were investigated for both electrical conductivity, changing temperatures and optical properties by UV-vis spectrometers. It was clear, as a result that electrical conductivity was increased by raising CNT rates for both groups. Beside composites containing CdO, synthesized by sol-gel method have higher conductivity than composites containing CdO bought by commercial have. To sum up, CdO composites synthesized by sol-gel have both higher conductivity and optical properties comparing with commercials have.

**Keywords:** Carbon Nanotube, Cadmium Oxide, Composite

## 1. INTRODUCTION

Cadmium oxide is used in metal-matrix semiconductor technology. Solar cells, gas sensors, liquid crystals and smart screens, optical heater and LED (Lighting Emission Diode) are the most important usage areas (Soylu *et al.*, 2015). CdO is the one of the important semiconductor in which metal-oxides field for optoelectronic devices (Gullino *et al.*, 2005). Owing to crystal structure and oxygen vacancies, CdO is an n-type semiconductor (Haul *et al.*, 1962). Both scientist and engineers are interested in due to 2.2 eV band gap (Ristic *et al.*, 2004; Jayakrishnan *et al.*, 2003). High transparency in visible lights, high conductivity in room temperature (Ristic *et al.*, 2004),  $10^{19}/\text{cm}^3$  (Zhou *et al.*, 2007) electron concentration, and also high mobility  $\mu=130\text{cm}^2/\text{V.s}$  (Cruz *et al.*, 2005) are became CdO special part of semiconductors. CdO can be produced for several different methods, for examples, chemical bath sediment deposition, sol-gel, sputtering, spray pyrolysis, solid liquid vapor.

After the discovery of CNT (Carbon Nanotube) by Iijima (1991), CNT was attracted scientist and manufacturer's attention due to its usability to several disciplines. The controllability at the nanoscale for materials led us to show different characteristics (Siegel *et al.*, 1999). These characteristics are played a huge role in different and wide industrial applications for instance high-strength composites, bioscience, nanoscale semiconductors and hydrogen storage (Saito *et al.*, 1998; Baughman *et al.*, 2002). Possession of excellent flexibility, very low density and having high conductivity (Wang *et al.*, 2013; Xining *et al.*, 2014) make CNT's application areas are diversified. Graphene has 1600 – 2400 GPa approximately Young Module, 120 – 140 GPa Tensile Strength and  $2 \times 10^5 \text{ cm}^2 \text{ V}^{-1} \text{ s}^{-1}$  approximately Carrier Mobility. These all are 270 – 950 GPa, 11 – 150 GPa respectively for Multi Walled Carbon Nanotubes and 1000 GPa approximately, 13 – 53 GPa,  $0.79 - 1.2 \times 10^5 \text{ cm}^2 \text{ V}^{-1} \text{ s}^{-1}$  respectively for Single Walled Carbon Nanotube (Xining *et al.*, 2014).

The method studying with obtained CdO commercially is very widespread. Besides this method, the new another method that gained nanoscale material by using Sol-Gel is gaining popularity. Sol-Gel is an advantageous method that emerges because of the traceability of morphologic and dimensional control of nano-sized materials to be synthesized (Wang *et al.*, 2013). Another advantage of this method is not only production of metal matrix materials, but also can be using production for organic-inorganic hybrid materials.

In our study, the C group samples stand for obtained CdO commercially, the S group of samples stand for gained CdO with Sol-Gel method. These groups are given a chance comparing with commercial CdO and Sol-Gel CdO.

## 2. EXPERIMENTAL

In this study, CdO was used as matrix material. Acros Organic brand (Code: 223792500, 99 % purity). The CNT used as a dopant was synthesized by Chemical Vapor Deposition (CVD) method. A single-crystal Silicon mat (100) was used in the CNT synthesis. Firstly, the mat was washed with acetone in ultrasonic bath. Secondly, washed

mat was washed again with ethanol in the same media. After the bath process, the mat was placed in middle of a tube furnace, on a button. The inside of the tube furnace was evacuated with a pump and was free of air. After those, was heated to 650 °C and Ar gas was used during the heating period. The Ar gas was given the system with 1 lt flow rate. Once tube furnace was 650 °C, cut the flow of Ar gas and acetylene gas ( $\text{C}_2 \text{H}_2$ ) was given for 40 minutes. The end of the 40 minutes, the flow of acetylene was cut down and Ar gas was given again until furnace temperature was down to room level.

First of all, CNT was added in to CdO which was obtained commercially, as 0.2, 0.5 and 1 % w. For the production of composite, carbon nanotubes gauged in a beaker in the appropriate weight and added alcohol on it. To a homogenous mixture alcohol carbon nanotube mixture was stirred in an ultrasonic stirrer and then added in appropriate amount of CdO. The fish is mixed magnetic stirrer until alcohol was evaporates. The resulting powder mixture was pressed into pellets at a pressure of 600 MPa and then was sintered at 450 °C. Code name is given to samples and they are shown in Table 1.

The structure of obtained composites was determined with Scanning Electron Microscope. Jeol Jsm 7001 F brand was used in this study. Electrical conductivity of the composites was measured using two-probe method with the help of Keithley 6517A Electrometer/High-Resistance Meter. Optical measurements of the samples were performed using a Shimadzu UV-3600 PC UV-VIS spectrophotometer.

Table 1. Code name of samples

Code	Composition of samples
C0	Pure commercial CdO
C1	0,2% CNT – CdO composite
C2	0,5 % CNT – CdO composite
C3	1 % CNT – CdO composite

## 3. RESULTS AND DISCUSSION

Fig. 1. a, b and c show SEM images for Pure CdO, % 0,2 CNT – CdO and % 1 CNT – CdO samples, respectively. As seen from these images, the homogeneous distribution in composite of CNTs were increasingly difficult with the increase in the CNT quantity of composite. In 0.2 % CNT reinforced specimen, CNTs were seldomly disitubed to structure. This state was arised from relatively few of CNTs quantity. Also, CNTs were homogenly disitubed to structure. Furthermore, In 0.1% CNT reinforced specimen, CNT bundles were completely dissolved. As seen from SEM images of 1 % CNT reinforced specimens, dissolve of CNT bundles and disperse of CNTs in strucure were relatively limited. In 1% CNT reinforced composite, CNTs wrap up alike a cobweb on CdO grains. In certain regions, it was seen that no CNTs bundles were dissolved and remain as cluster. In study, The common features of all CNT reinforced specimens are that shortening of CNTs length were occurred. This state arise because of applied ball milling in order to disperse uniformly in structure and applied mild sonication in order to dissolve the CNT bundles. Breaking of CNTs was occurred during these processes.

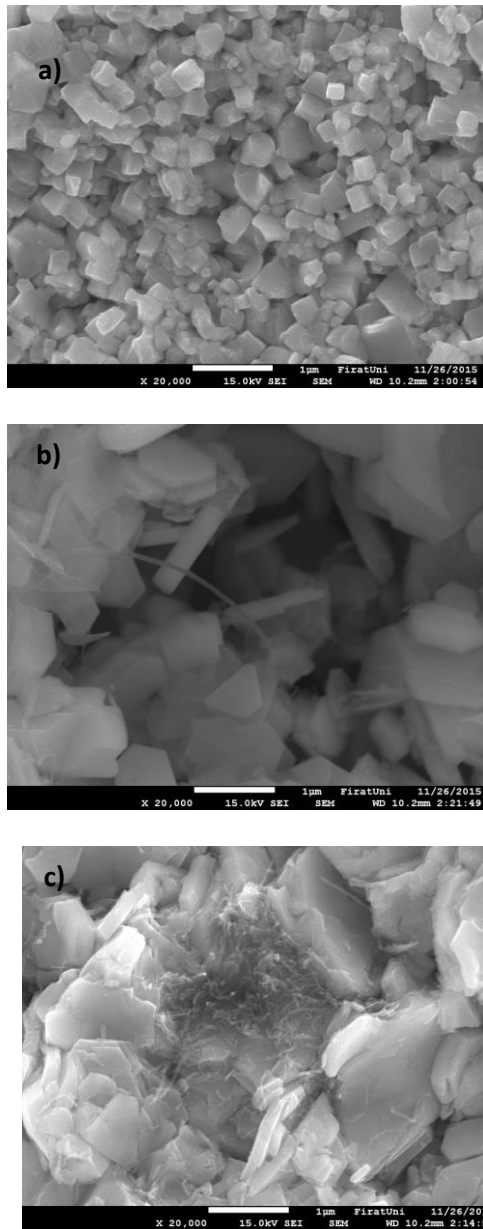


Fig. 1. a) Pure CdO b) 0.2 wt % CNT c) 1 wt % SEM images of the composites

The electrical transport operation of CNT-CdO composites were studied by the temperature dependent conductivity. As seen in Fig. 2, the electrical conductivity of the composites increases with increasing temperature. But, electrical conductivity of pure CdO is constant with increasing temperature. It is observed that the conductivity of the CdO based composite increased with increasing CNT content. The reason of the increase in conductivity with the increase in temperature is due to the loaded carriers exceeding the activation energy barrier of the CdO based composites. Elevated temperatures cause an increase in the number of charge carriers involved in electrical conduction (Güler *et al.*, 2015).

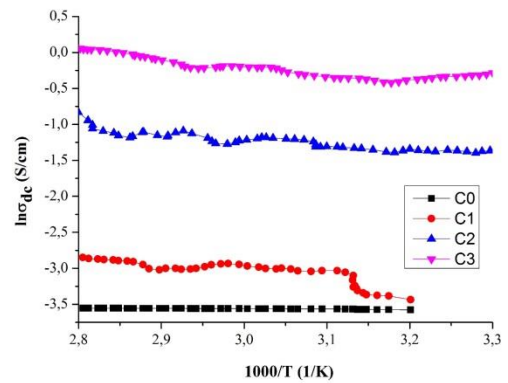


Fig. 2. Plots of the electrical conductivity versus temperature of the CNT-CdO nanocomposites

Fig. 3 show the plots of the diffused reflectance for undoped and CNT-reinforced CdO composites, respectively. The reflectance of the 0,2%, 0,5% and 1% CNT reinforced specimens point out a rise at 300 nm, 310 nm, 295 nm, respectively. The reflectance of the composites is firstly increased, then decreased with CNT contents. But, composites reflectance values decrease in comparison with pure CdO. The decrease in reflectance is due to the increase in absorbance of the composites. Additionally, the change in reflectance of the samples with CNT dopants is resulted from the surface and the internal reflection effects of the composites, because, when CNT into composite is added, it changes the color and surface properties of the composite. As a result the absorption of the samples is increased and the reflectance is reduced depending on the amount of CNT.

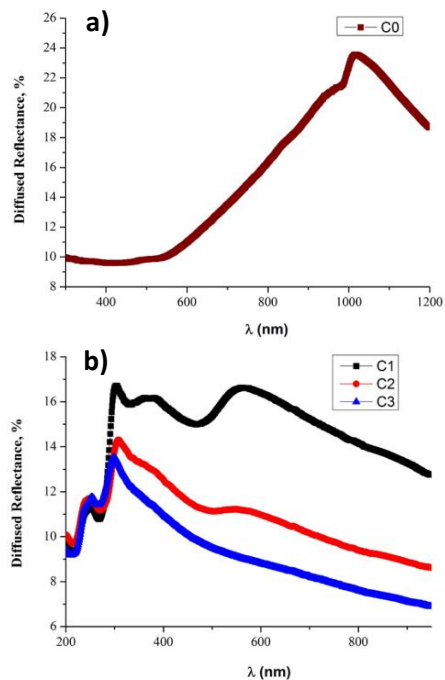


Fig.3. The reflection spectrum of (a) undoped and (b) CNT-CdO nanocomposites

The optical band gaps of the composites were determined by optical reflection method based on Kubelka-Munk for the analysis of diffuse reflection spectra. The Kubelka-Munk theory is obtained for the analysis of diffuse reflectance spectra from a weak absorptive sample. The reflection spectrum of the compounds shows that the composites prepared are a gently absorbing material. The Kubelka-Munk function can be expressed by the following formula (Aydin *et al.*, 2011).

$$F(R) = \frac{(1-R)^2}{2R} \quad (1)$$

Here, F (R) is the Kubelka-Munk function corresponding to the absorbance and R is the reflection. The reflection spectrum of undoped and CNT-CdO nanocomposites are shown in Fig.3. To determine the optical band gaps of composites, the reflectance values were converted to absorbance. The Kubelka-Munk function is used for this. As a result, the relationship used to determine the optical band gaps of conventional semiconductors is as follows (Yakuphanoglu *et al.*, 2009).

$$F(R)h\nu = A(h\nu - E_g)^n \quad (2)$$

Where A is a constant and  $E_g$  is the optical band gap, n is a constant exponent which determines the type of optical transitions. The optical band gap of the composites was determined from the plots of  $(F(R)h\nu)^2$  versus  $h\nu$ , as shown in Fig. 4.

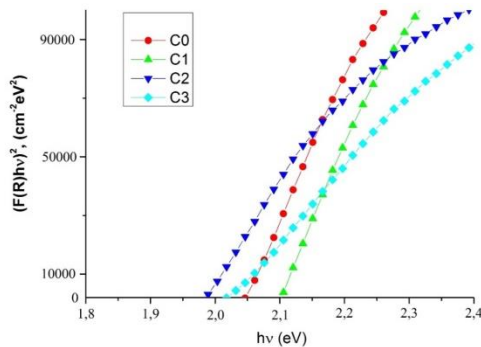


Fig. 4. Plots of  $(F(R)h\nu)^2$  versus the photon energy ( $h\nu$ ) of the CNT/CdO nano-composites.

Accordingly, the values of band gap of C group samples are changed to in Table 2. According to the table, while there was a decrease between C0 and C2 samples, an increase in C3 was observed.

Table 2. Band gap of C group samples

C Group	$E_g$ (eV)
C0	2,05
C1	2,1
C2	1,99

## CONCLUSION

As a result, CdO-CNT composites have been successfully produced. Homogeneous distribution in the CdO becomes more difficult by increasing the number of nanotubes. The electrical conductivity of the composites increased by increasing the amount of CNT and temperature. The optical absorption of the composites is around 295-310 nm. The optical band gap of samples is decrease with CNT contents.

## REFERENCES

- Aydin C., El-Nasser H.M, Yakuphanoglu F., Yahia I.S., Aksoy M. (2011). "Nanopoweder Synthesis of Aluminum Doped Cadmium Oxide Via Sol-Gel Calcination Processing", *Journal of Alloys and Compounds*, Vol.509, pp. 854-858.
- Baughman R.H., Zakhidov A.A., Heer W.A. De., (2002). "Carbon Nanotubes--The Route Toward Applications", *2 August Science*, Vol.297, No.5582, pp.787-792.
- Cruz J.S., Delgado G.T., Perez R.C., Sandoval S.J., Sandoval O.J., Romero C.I.Z., Marin J.M., Angel O.Z. (2005). "Dependence of Electrical and Optical Properties of Sol-Gel Prepared Undoped Cadmium Oxide Thin Films on Annealing Temperature", *Thin Solid Films*, Vol.493, pp.83-87.
- Gullino A., Tabbi G., (2005) "Cdo Thin Films: A Study of Their Electronic Structure By Electron Spin Resonance Spectroscopy.", *Applied Surface Science*, Vol. 245, pp.322-327.
- Güler Ö, Güler S.H, Yakuphanoglu F., Aydın H., Aydın C., El-Tantay F.,El Shazly, Duria M.and Fonda A.N. (2015). "Electical and optical properties of Carbon Nanotube Hybrid Zinc Oxide Nanocomposites Prepared by ball mill technique" *Fullerenes, Nanotubes and Carbon Nanostructures*, Vol.23, pp.865-869.
- Haul R., D. Just. (1962). "Disorder And Oxygen Transport In Cadmium Oxide.", *Journal of Applied Physics*, Vol. 33, pp.487-493.
- Iijima, S. (1991). "Helical Microtubules of Graphitic Carbon", *Nature*, 354, pp.56-58.
- Jayakrishnan R., Hodes G. (2003). "Non-Aqueous Electrodeposition of ZnO and CdO Films", *Thin Solid Films*, Vol. 440, pp.19-25.
- Ristic M, Popovic S., Music S. (2004). "Formation And Properties of Cd(OH)<sub>2</sub> and CdO Particles.", *Materials Letters*, Vol.58, pp. 2494 - 2499.
- Saito R., Dresselhaus G., Dresselhaus M.S. (1998). "Physical Properties of Carbon Nanotubes", *Imperial College Press*, London.
- Siegel R.W., Hu E., Roco M.C. (1999). "Nanostructure Science and Technology, A Worldwide Study", *National*

*Science and Technology Report*, WTEC, Loyola College, Maryland.

Soylu., M., Al-Ghamdi A., Yakuphanoglu F. (2015). "Transparent CdO/N-GaN(0001) Heterojunction for Optoelectronic Applications." *Journal of Physics and Chemistry of Solids*, Vol.85, pp.26–33.

Wang K., Lou S., Y. Wu, X. He, F. Zhao, J. Wang, K. Jiang, S. Fan. (2013). "Super-Aligned Carbon Nanotube Films As Current Collectors For Lightweight And Flexible Lithium Ion Batteries", *Advanced Functional Materials*, Vol. 23, No.7, pp. 846-853.

Xining Z., Qin Z., Jinyoung C., Yumeng L., Liwei L. (2015) "Graphene and Carbon Nanotube (CNT) In Mems/Nems Applications", *Microelectronic Engineering*, Vol. 132,pp. 192–206.

Yakuphanoglu F., Mehrotra R., Gupta A., Munoz M. (2009). "Nanofiber organic semiconductors: The effects of nanosize on the electrical charge transport and optical properties of bulk polyanilines" *Journal of Applied Polymer Science*, Vol.114, pp.794-799.

Zhou Q., Ji Z., Hu B., Chen C., Zhao L., Wang C. (2007). "Low Resistivity Transparent Conducting CdO Thin Films Deposited by DC Reactive Magnetron Sputtering at Room Temperature", *Mater. Lett.*, Vol. 61, pp.531–534.

Copyright © Turkish Journal of Engineering (TUJE).  
All rights reserved, including the making of copies  
unless permission is obtained from the copyright  
proprietors.

# Turkish Journal of Engineering



*Turkish Journal of Engineering (TUJE)*  
*Vol. 1, Issue 2, pp. 66-69, September 2017*  
*ISSN 2587-1366, Turkey*  
*DOI: 10.31127/tuje.316855*  
*Research Article*

## **DESIGNING A COMPACT MONOPOLE MICROSTRIP ANTENNA OPERATING AT ULTRA-WIDE BAND FOR MICROWAVE IMAGING APPLICATIONS**

Mustafa Berkan Biçer<sup>1</sup> and Ali Akdağlı<sup>\*2</sup>

<sup>1</sup> Mersin University, Engineering Faculty, Department of Electrical and Electronics Engineering, Mersin, Turkey  
(mbbicer@gmail.com)

<sup>2</sup> Mersin University, Engineering Faculty, Department of Electrical and Electronics Engineering, Mersin, Turkey  
(akdagli@mersin.edu.tr)

---

\* Corresponding Author

Received: 29/03/2017      Accepted: 22/05/2017

---

### **ABSTRACT**

In this paper, a novel design of a microstrip-fed compact monopole microstrip antenna with asymmetrically modified ground plane operating at ultra-wide band (UWB) frequency range is presented for microwave imaging applications. The performance characteristics of the proposed antenna in terms of impedance bandwidth and return loss meet the ultra-wide band requirements. The design and simulation procedures of the proposed antenna are carried out using an electromagnetic simulation software based on the characteristic impedance for the transmission line model. The proposed antenna, with small size of  $32 \times 42 \times 1.55 \text{ mm}^3$  on an FR4 epoxy substrate with permittivity ( $\epsilon_r$ ) 4.4, is fabricated and validated through the simulations and measurements. It is demonstrated that the measured -10 dB bandwidth for return loss is from 2.08 to 7.4 GHz but after this frequency, the antenna operates with minimum 87.4% efficiency up to 10.6 GHz. The antenna exhibits acceptable UWB characteristics and the results show that the designed antenna is suitable for various microwave imaging applications operating at UWB.

**Keywords:** *Microstrip, Antenna, Monopole, UWB, Imaging*

## 1. INTRODUCTION

In the last decades, the interest in microstrip antennas (MA) has increased with the development of technology and the miniaturization of wireless communication devices. Due to their attractive features such as simple structure, low profile, low cost, planar configuration, conformal shaping, ease in fabrication and integration with microwave integrated circuits and solid-state devices, microstrip antennas have been widely implemented with the development of ultra-wide band (UWB) applications such as mobile phones, personal communication systems (PCS), mobile satellite communications (MSC), direct broadcast satellite (DBS), wireless local area networks (WLAN) and other wireless and mobile devices that demand small sized antennas (Balanis, 2005). Besides, MA's are also preferred in applications such as ground penetrating radar, parking radars, indoor positioning, military applications and medical imaging.

Since 2002, Federal Communication Commission (FCC) of United States authorized the use of the frequency range from 3.1 GHz to 10.6 GHz for unlicensed use for UWB based on wideband to transmit data at very low power and the researchers have been focused on the design, research and development of UWB antennas to achieve the UWB technology requirements. UWB is defined as a technology that requires either a bandwidth of 500 MHz or fractional bandwidth equal to or greater than 20%.

Because of the ease in analysis and design, a significant part of the studies on patch antennas presented in the literature have concentrated on conventional MA geometries such as rectangular, triangular and circular. However, conventional shaped MAs have some drawbacks such as narrow impedance bandwidth, low efficiency, low gain and low power handling. Also, regularly shaped MAs are larger in size for lower frequencies. To overcome these disadvantages, compact microstrip antennas (CMAs) are proposed by modifying the MAs having conventional geometries mentioned above.

There are various techniques such as modifying the ground plane, slot loading on the ground and radiating patch, changing feeding techniques and using parasitic elements with stacked superstrates to achieve enhanced bandwidth and provide a reduction in antenna size. Due to their regular geometries, the transmission line model (Bhattacharyya et. al., 1985) and cavity model (Richards et. al., 1981) are utilized in the analysis of the conventional shaped MAs. On the other hand, the irregular structures of CMAs lead to difficulty and complexity in theoretical calculations. To overcome this problem, electromagnetic methods covering proper mathematical expressions with considerable numerical procedures such as finite difference time domain (FDTD) method (Taflou, 2005), finite element method (FEM) (Arora et. al., 2013) and method of moment (MoM) (Harrington, 1993) are extensively employed.

In the literature, various studies on CMA designs for microwave imaging applications operating at UWB are available and they can be used with their own benefits and limitations. Ghassemi et al. (2008) proposed a microstrip antenna design using two slots operating from 9.8 GHz to 19 GHz with a simulated gain of 5 dB. Compact microstrip patch antenna for UWB applications operating

between 3 GHz and 10.26 GHz frequency band is designed by Mazhar et al. (2013) and measurement results are presented. Popovic and Kanj (2008) designed a new design of an ultra-compact broadband antenna for microwave breast tumor detection with -10 dB return loss bandwidth from 2 GHz to 35 GHz band. Another miniaturized microstrip antenna having T-slot operating between 2.85 GHz and 13.21 GHz frequency band for microwave imaging is proposed by Karli et al. (2014).

In this paper, a new design of a microstrip-fed compact monopole microstrip antenna with asymmetrically modified ground plane operating at ultra-wide band (UWB) frequency range is proposed. The asymmetric radiating element geometry provides 10 dB bandwidth between 2.08 GHz and 7.4 GHz and 9 dB bandwidth between 2 GHz and 8.5 GHz according to measurement results. The designed antenna with small size of  $32 \times 42 \times 1.55 \text{ mm}^3$  on an FR4 epoxy substrate with permittivity ( $\epsilon_r$ ) 4.4 is fabricated. The simulation and measurement results show that the proposed antenna is a suitable choice for microwave imaging applications because of its small structure and low power handling performance.

## 2. ANTENNA DESIGN

The configuration of the designed antenna structure for microwave imaging applications, shown in Fig. 1, has a microstrip-fed asymmetric radiating patch with 18 nodes and an asymmetric ground plane.

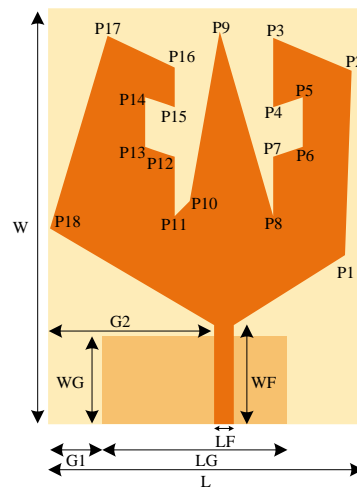


Fig. 1. The proposed antenna.

The width and length of the substrate and initial design are chosen to obtain minimum resonance frequency and tapered parts are used to maximize the impedance matching possibility. The ground plane is modified by reducing size and shifting to left to achieve UWB bandwidth requirements. The ground plane parameters and nodes of the radiating element are chosen to be optimized with the use of Particle Swarm Optimization (PSO) algorithm (Minasian et. al., 2013) to provide best impedance bandwidth. The physical parameters obtained by optimizing the structure of the designed antenna are given in Table 1.

Table 1. Physical parameters of the proposed antenna

Parameter	Value
L	32 mm
W	42 mm
LF	2 mm
WF	8.79 mm
LG	16.99 mm
WG	8.03 mm
G1	4.11 mm
G2	14 mm
P1	(31.33 mm, 16.31 mm)
P2	(31.25 mm, 37.06 mm)
P3	(23 mm, 39 mm)
P4	(23 mm, 32 mm)
P5	(26 mm, 33 mm)
P6	(26 mm, 28 mm)
P7	(23 mm, 27 mm)
P8	(23.58 mm, 19.32 mm)
P9	(18.23 mm, 31.51 mm)
P10	(13.65 mm, 40.18 mm)
P11	(12.82 mm, 22.89 mm)
P12	(13 mm, 27 mm)
P13	(10 mm, 28 mm)
P14	(10 mm, 33 mm)
P15	(13 mm, 32 mm)
P16	(13 mm, 36 mm)
P17	(1.41 mm, 36.84)
P18	(0.68 mm, 17.22 mm)

The proposed antenna has three irregular-shaped branch strips to shape return loss results for UWB frequency range. The antenna is fed by a microstrip line of width  $WF = 8.79$  mm and length  $LF = 2$  mm. The ground plane is placed asymmetrically on the other side of the FR4 epoxy substrate with permittivity of 4.4 and thickness of 1.55 mm. The outer dimensions of the substrate are chosen as  $32 \times 42$  mm<sup>2</sup>. The feed structure of the proposed antenna is chosen as microstrip-fed and the feed line is formed to match characteristics impedance of  $50 \Omega$ .

### 3. NUMERICAL RESULTS

The photograph of the fabricated antenna is given in Fig. 2. The antenna is fabricated by scraping the copper planes to form the designed geometries of the radiating element and ground element on an FR4 epoxy substrate using LPKF E33 PCB prototyping machine. The return loss results of the fabricated antenna are measured by Agilent E5071B ENA Series RF Network Analyzer. The measured results of the antenna are limited to the lower and upper frequencies of 2 GHz and 8.5 GHz, respectively, because the network analyzer can measure up to 8.5 GHz frequency.

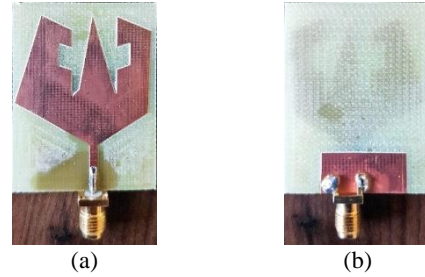


Fig. 2. (a) Top view and (b) bottom view of the fabricated antenna.

The comparison of the simulated and measured return loss of the fabricated antenna is given in Fig. 3.

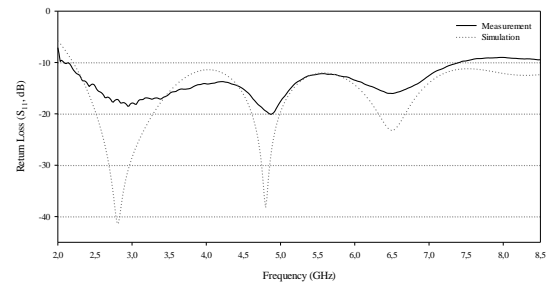


Fig. 3. Comparison of the simulated and measured return loss of the proposed antenna

It can be seen from the Fig. 3 that the simulation and measurement results are in a good agreement in overall frequency regions and the measured results are below -10 dB between 2.08 GHz and 7.4 GHz. Since the return loss represents the ratio of the reflected power to the transmitted power, the antenna can operate with lower efficiencies above -10 dB reference. The calculated efficiency using measured return loss is minimum 87.4%.

The simulated radiation pattern of the designed antenna is given in Fig. 4.

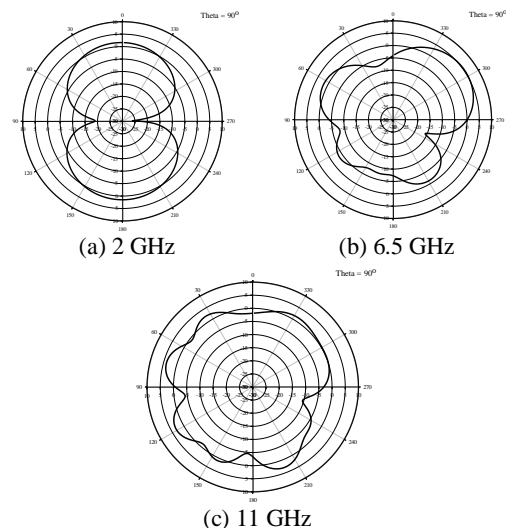


Fig. 4. The simulated radiation patterns for  $\theta = 90^\circ$  at (a) 2 GHz, (b) 6.5 GHz and (c) 11 GHz.

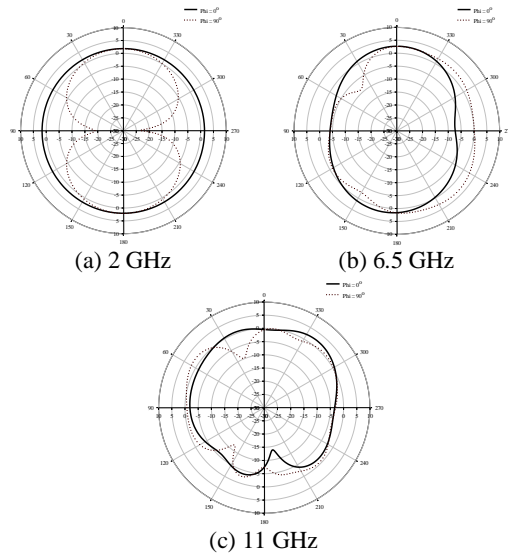


Fig. 5. The simulated radiation patterns for  $\phi = 0^\circ$  (solid) and  $\phi = 90^\circ$  (dashed) at (a) 2 GHz, (b) 6.5 GHz and (c) 11 GHz.

It can be seen from the Fig. 4 that the radiation pattern of the proposed antenna has a 3D donut shape and approximately bi-directional in the lower range of the UWB band. The change in the radiation diagram in the x-y plane and the appearance of side lobes with the increase in frequency are shown in Fig. 4 (b) and (c). Besides, the radiation characteristics of the proposed antenna in the y-z plane are nearly bi-directional whole UWB band.

## 5. CONCLUSION

A novel and compact monopole microstrip antenna with asymmetrically modified ground plane and microstrip-fed operating at UWB range for microwave imaging applications is presented. The designed antenna is fabricated on an FR4 epoxy substrate with permittivity ( $\epsilon_r$ ) of 4.4 and size of  $32 \times 42 \times 1.55 \text{ mm}^3$ . The experimental results are compared with the simulated ones and it is seen that simulation and experimental results are in a good agreement. It is concluded that the proposed design is useful for microwave imaging applications and may be useful for microstrip antenna designers for specific fields and microwave imaging researchers.

## ACKNOWLEDGEMENTS

This study was supported by the Research Fund of Mersin University in Turkey with Project Number: 2017-1-TP3-2190.

## REFERENCES

- Arora, R., Kumar, A., Khan, S. and Arya, S. (2013). "Finite element modeling and design of rectangular patch antenna with different feeding techniques." *Open Journal of Antennas and Propagation*, Vol. 1, pp. 11-17.
- Balanis, C. A. (2005). *Antenna theory: analysis and design*, Wiley Interscience.

Bhattacharyya, A. K. and Garg, R. (1985). "Generalized transmission line model for microstrip patches." *IEEE Proc. Microwave Antennas Propagation*, Vol. 132, No. 2, 93-98.

Bicer, M. B. and Akdagli, A. (2012). "A novel microstrip-fed monopole antenna for WLAN/WiMAX applications." *J. of Electromagn. Waves and Appl.*, Vol. 26, pp. 904-913.

Ghassemi, N., Rashed-Mohassel, J. and Neshati, M. H. (2008). "Microstrip antenna design for ultra wideband application by using two slots." *Progress In Electromagnetics Research Symposium*, Hangzhou, China, pp. 159-161.

Harrington, R. F. (1993). *Field computation by moment methods*, Wiley - IEEE Press, NJ.

Kanj, H. and Popovic, M. (2008). "A novel ultra-compact broadband antenna for microwave breast tumor detection." *Progress In Electromagnetics Research*, Vol. 86, pp. 169-198.

Karli, R. and Ammor, H. (2014). "Miniaturized UWB microstrip antenna with T-slot for detecting malignant tumors by microwave imaging." *International Journal of Microwave and Optical Technology*, Vol. 9, No. 3, pp. 214-220.

Mazhar, W., Tarar, M. A., Tahir, F. A., Ullah, S. and Bhatti, F. A. (2013). "Compact microstrip patch antenna for ultra-wideband applications." *PIERS Proceedings*, Stockholm, Sweden, pp. 1100-1104.

Minasian, A. A. and Bird, T. S. (2013). "Particle swarm optimization of microstrip antennas for wireless communication systems." *IEEE Transactions on Antennas and Propagation*, Vol. 61, No. 12, pp. 6214-6217.

Richards, W. F., Y. T. Lo, and Harrison, D. D. (1981). "An improved theory for microstrip antennas and applications." *IEEE Trans. Antennas Propagation Magazine*, Vol. 29, pp. 38-46.

Taflove, A. (2005). *Computational electrodynamics: the finite difference time domain method*, Artech House, London.

Copyright © Turkish Journal of Engineering (TUJE). All rights reserved, including the making of copies unless permission is obtained from the copyright proprietors.

# Turkish Journal of Engineering



*Turkish Journal of Engineering (TUJE)*  
*Vol. 1, Issue 2, pp. 70-75, September 2017*  
*ISSN 2587-1366, Turkey*  
*DOI: 10.31127/tuje.316254*  
*Research Article*

## **FABRICATION OF Cu-Al-Ni SHAPE MEMORY THIN FILM BY THERMAL EVAPORATION**

Canan Aksu Canbay <sup>\*1</sup>, Ayşe Tekataş <sup>2</sup> and İskender Özkul <sup>3</sup>

<sup>1</sup> Firat University Faculty of Science, Department of Physics, Elazığ, Turkey  
(caksu@firat.edu.tr)

<sup>2</sup> Firat University Faculty of Science, Department of Physics, Elazığ, Turkey  
(atekatas@firat.edu.tr)

<sup>3</sup> Mersin University, Engineering Faculty, Department of Mechanical Engineering, Mersin, Turkey  
(iskender@mersin.edu.tr)

---

\* Corresponding Author

Received: 13/04/2017      Accepted: 23/05/2017

---

### **ABSTRACT**

Among the functional, materials shape memory alloys are important because of their unique properties. So, these materials have attracted more attention to be used in micro/nano electronic and electromechanic systems. In this work, thermal evaporation method has been used to produce CuAlNi shape memory alloy thin film. The produced CuAlNi thin film has been characterized and the presence of the martensite phase was investigated and compared with the CuAlNi alloy sample. CuAlNi shape memory alloy thin film about 6.12  $\mu\text{m}$  thick, showing a M $\rightarrow$ A transformation has been produced and also thermal and structural observations were made to analysis the shape memory behaviour of the Cu-Al-Ni shape memory thin films.

**Keywords:** *Thin films, Shape memory effect, Cu-Al-Ni, Microstructure.*

## 1. INTRODUCTION

Shape memory alloys (SMAs) have attracted considerable interest for mechanical, engineering and medical applications owe to their unique functional properties such as shape memory effect (SME) and superelasticity (SE) (Wang, Zu et al. 2006). SMAs exhibit two different phases, which are called austenite phase and martensite phase. Austenite phase is known as high temperature phase and martensite phase is known as low temperature phase. Austenite and martensite phase start and finish temperatures are named as  $A_s$ ,  $A_f$ ,  $M_s$  and  $M_f$ , respectively (Karagoz and Canbay, 2013). The shape memory effect describes the shape memory via temperature-induced transformation and superelasticity describes the shape memory via stress-induced transformations (Massad and Smith 2005). In some applications both stress and temperature can be affected the transformation of these materials (Recarte, Perez-Landazabal et al. 2004, Lojen, Anžel et al. 2005, Canbay 2010, Izadinia and Dehghani 2011, Kato, Yasuda et al. 2011, Sobrero, La Roca et al. 2012).

SMAs have a diffusionless and first order transformation characterized by an atomic shearing of the crystal lattice from at high temperature to low temperature, which present characteristic structural domains, called martensite variants. Cu-based SMAs show order-disorder phase transitions from high-symmetry crystal structure (at high temperature) to low symmetry crystal structure (at low temperature) (Otsuka and Wayman 1998, Gómez-Cortés, San Juan et al. 2013). Due to the high working capability of SMAs, they have attracted much attention to be used in micro/nano electromechanical systems. So these materials acquired more attention in technological developments. According to this factor, there has been a significant research focused on SMA thin films that could be used in microsystems (Otsuka and Ren 2005).

Thin film fabrication from Cu-Al-Ni SMA has also been the aim of this research. In this work, Cu-Al-Ni thin film produced by thermal evaporation and also thermal and structural observations were made to analysis the shape memory behaviour of the Cu-Al-Ni shape memory thin film. In addition to this, we compare the thermal and structural observation results of the SMA with thin film.

## 2. EXPERIMENTAL

The sample was prepared from the high purity of Cu (99.9 %), Al (99.9 %) and Ni (99.9 %) elements, and melted in arc melter furnace under vacuum. The obtained sample was cut from the cast ingot, and the specimens were solution-treated at 850 °C in  $\beta$ -phase region for 1 h, and then quenched in iced-brine water to obtain the  $\beta_1$  martensite phase. Then a piece of the homogenized sample was deposited on Si substrate by thermal evaporation method under  $4 \times 10^{-5}$  T vacuum. The alloy sample and the thin film images are given in Figure 1. For the analysis of alloy sample, the characteristic transformation behaviours were determined with 5, 15, 25 and 35 °C/min. heating/cooling rates (Shimadzu DSC-60A differential scanning calorimetry) and for the thermal analysis of the thin film 15 °C/min heating/cooling rate was used. The TG/DTA (Shimadzu TA-60 WS) measurements were performed from room temperature to 1000 °C at a heating rate of 20 °C/min to

identify order-disorder phase transitions at high temperatures. The chemical compositions of the alloy and thin film (Table 1) were examined by Bruker Model energy dispersive X-ray (EDX). X-Ray diffraction patterns of the samples were taken by Rigaku RadB-DMAX II diffractometer. For these examinations, the monochromatic copper  $K\alpha$  radiation with wavelength of 1.5405 Å was used. After the EDX and X-ray analysis, the alloy sample was etched by using a solution consisting of 5g (FeCl<sub>3</sub>-6H<sub>2</sub>O)-96 ml methanol with 20ml HCl. The surfaces of the alloy sample and thin film were characterized by Nikon MA200 model optical metallographic microscope. And the thickness of the thin film was observed by scanning electron microscope SEM (LEO evo 40 Model) as 6.12 µm.

Table 1. Chemical compositions of the alloy and thin film (wt. %).

Alloy ID	Cu	Al	Ni
Alloy	82.04	14.60	3.36
Thin film	86.77	11.46	1.77



Fig. 1. The images of Cu-Al-Ni alloy sample and thin film.

## 3. RESULTS AND DISCUSSION

The alloy sample and the thin film of Cu-Al-Ni were thermally analysed by DSC measurements under nitrogen atmosphere. For the alloy sample 5, 15, 25 ve 35 °C/min. heating/cooling rates were used to determine the austenite→martensite and Fig. 2 illustrates the martensite→austenite phase transitions. DSC studies of the alloy sample have shown that the position of the direct and reverse martensitic transformation peaks remain stable with the thermal cycling occurred during the measurement of the different heating rates. And also the hysteresis observed from the DSC analysis, is one of the typical characteristics of the thermoelastic martensitic transformations. During this transformation, nucleation process occurred rapidly and the activation energy of this transformation is very small (Canbay 2010, Karagoz and Canbay 2013). The characteristic transformation temperatures of high temperature phase and low temperature phase such as  $A_s$ ,  $A_f$ ,  $M_s$  and  $M_f$  of the samples are determined, where the DSC curve deviates from linearity. The obtained results from the DSC measurements for the alloy sample are given in Table 2. When we compare the characteristic transformation temperatures of fabricated Cu-14.6 Al-3.36 Ni (% wt.) with the Cu-14 Al-4 Ni (% wt.), Cu-13.3 Al-4.0 Ni (%

wt.) and Cu-13 Al-4 Ni (% wt.), the transformation temperatures of the investigated alloy is low. On the other hand, according to Cu-13.5 Al-4 Ni (% wt.) and Cu-13.83 Al-2.34 Ni (% wt.) the transformation temperatures of the investigated alloy is high. As a result of this, we can assume that in Cu-Al-Ni system aluminium is also affected the characteristic transformation temperatures and especially aluminium is more effective than copper in binary Cu-Al system. So, the aluminium is dominant on the characteristic transformation temperatures in Cu-Al-Ni system then nickel. The change in Af-Ms hysteresis is shown in Fig. 3 and the hysteresis increases with the increase of the heating/cooling rate. This is a well-known situation in SMA systems, that the increase of heating/cooling rate also effects the transformation temperatures (Canbay 2010).

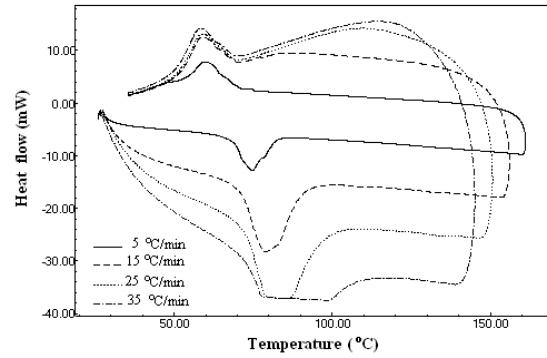


Fig. 2. DSC curves of Cu-Al-Ni alloy sample with 5, 15, 25, 35 °C/min. heating/cooling rates.

Table 2. Characteristic transformation temperatures and thermodynamic parameters of Cu-Al-Ni alloy.

Heating/cooling rate (°C/min.)	As (°C)	Af (°C)	Amax (°C)	Ms (°C)	Mf (°C)	Mmax (°C)	$\Delta H_{M \rightarrow A}$ (J/g)	$\Delta H_{A \rightarrow M}$ (J/g)
5	68,47	82,38	74,70	66,90	54,45	60,27	-8,19	8,69
15	71,36	90,29	79,05	70,88	40,06	58,97	-9,69	5,01
25	72,17	96,10	86,35	68,75	51,52	58,60	-8,99	5,65
35	59,16	118,83	90,16	69,84	45,07	58,33	-5,18	5,83

The absorbed and released energy during heating and cooling related to the enthalpy values of austenite and martensite phases. So the energy required for the low temperature (martensite phase) and high temperature (austenite phase) transitions varied with the variation of the heating and cooling rates. As seen in Fig. 4 and Fig. 5 the enthalpy change during heating and cooling is given for the alloy sample. For the thin film, we cannot detect enthalpy values according to different heating and cooling rates.

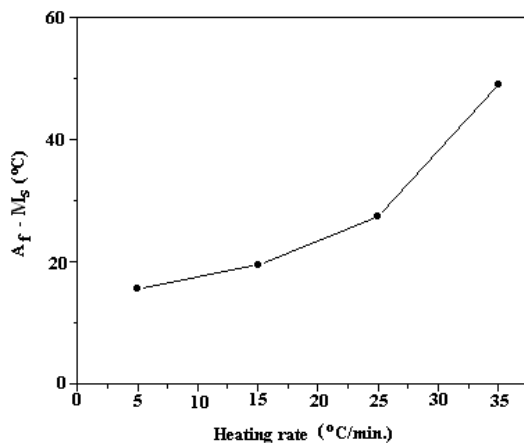


Fig. 3. The variation of (As-Ms) hysteresis versus heating/cooling rate.

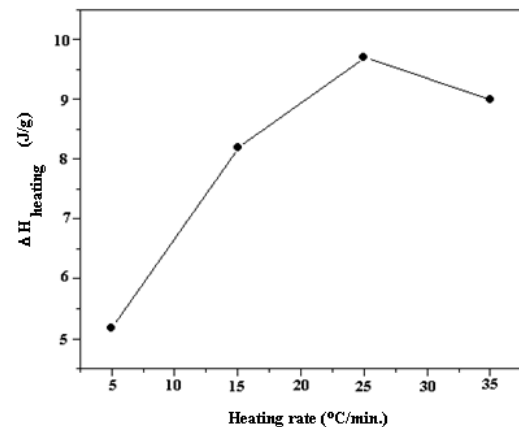


Fig. 4. The variation of enthalpy during heating ( $\Delta H_{\text{heating}}$ ) versus heating/cooling rate.

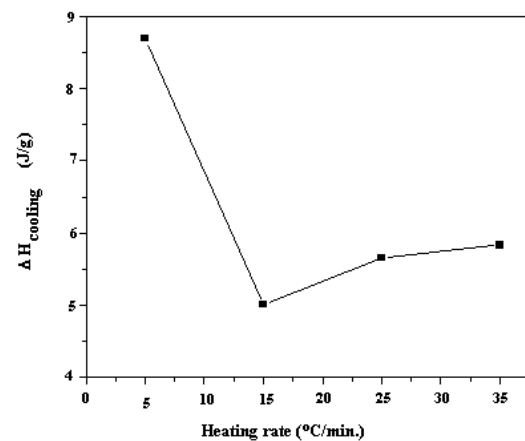


Fig. 5. The variation of enthalpy during cooling ( $\Delta H_{\text{cooling}}$ ) versus heating/cooling rate.

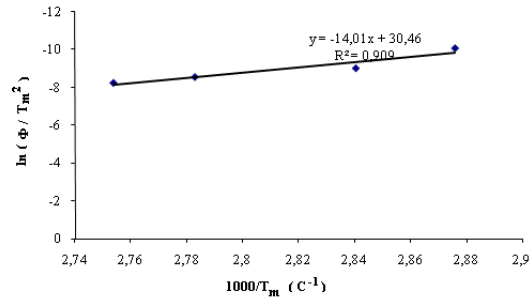
The activation energy values according to Kissinger and Ozawa methods are calculated to determine the kinetic parameters of the alloy sample. The activation energy value processed with the following equation developed by Kissinger (Kissinger 1957):

$$\frac{d[\ln(\phi/T_m^2)]}{d(1/T)} = -E/R \quad (1)$$

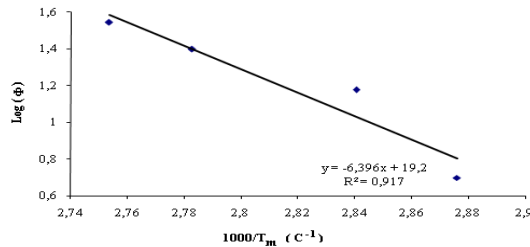
where  $\phi$  is the heating rate,  $T_m$  is the maximum temperature of the DSC peak,  $R$  is the universal gas constant, and  $E$  is the activation energy and according to Ozawa (1970):

$$E = \frac{-R}{b} \left[ \frac{d(\log \phi)}{d(1/T_m)} \right] \quad (2)$$

where  $b$  is a constant (0.4567). The activation energy values were calculated for the reverse transformation according to Kissinger and Ozawa methods and are 116,48 kJ/mol and 116,33kJ/mol, respectively. When we compare the activation energy values of the alloy sample according to the Kissinger and Ozawa methods independently, the values of both methods are the same. The activation energy of the thin film was not determined because only one heating/cooling rate can be used for the thermal analysis.



(a)



(b)

Fig. 6. Activation energy curves of the alloy sample; a) Kissinger, b) Ozawa methods.

The DSC curve of the thin film is given in Fig.7. As seen from the figure only martensite→austenite phase transition was observed and the reverse transformation was not detected. This is mainly due to the low weight

percentage of the thin film put into pans for the thermal analysis. Because it is well known that appropriate alloy concentration is required for a good shape memory effect. But for the thermal analysis of the thin film, it is evident that the appropriate alloy concentration is not been provided so we can only observed A→M phase transition. In addition to this, only one heating/cooling rate was used to determine the phase transition of the thin film and the thermodynamic parameters obtained from the thermal analysis is given in Table 3.

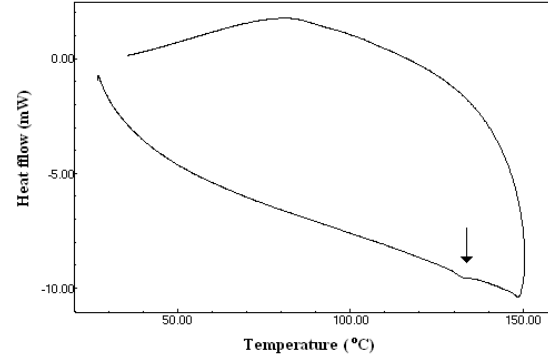


Fig. 7. DSC curve of the thin film. with a heating/cooling rate of 15 °C/min.

Table 3. Characteristic transformation temperatures and thermodynamic parameters of thin film.

Heating/cooling rate (°C/min.)	A <sub>s</sub> (°C)	A <sub>f</sub> (°C)	A <sub>max</sub> (°C)	ΔH <sub>M→A</sub> (J/g)
15	129,10	141,34	122,95	-0,56

The diffraction patterns of the alloy sample and thin film are given in Fig. 8. The main peak of the martensite phase, which was observed in both alloy and thin film is (0018). And (0018) plane is one of the main phase of martensite at room temperature. An interesting observation in XRD patterns, is the peaks laid between 2θ=35° to 45° that represented martensite structures formed. These planes have monoclinic crystal symmetry and the lattice parameters are a=4.420 Å b=5.260 Å and c=37.89 Å. The calculated a/b ratio is 0.84 and this value is smaller than  $\sqrt{3}/2$ . This indicates that, the main phase of the alloy and thin film is ordered and the atoms in the planes are in different sizes (Xuan, Bohong et al. 1987, Pérez-Landazábal, Recarte et al. 2006, Meng, Yang et al. 2010). The diffraction planes of the observed alloy sample and the thin film is the generally observed peaks in Cu-Al-Ni shape memory alloys and belong to M18R structure (Xuan, Bohong et al. 1987, Canbay 2010, Meng, Yang et al. 2010).

The average crystallite size (D) for the alloy and thin film was determined by Debye-Scherrer equation (Izadinia and Dehghani, 2011).

$$D = \frac{0.9\lambda}{B_{\frac{1}{2}} \cos \theta} \quad (3)$$

where  $\lambda$  is the wavelength of the X-ray (CuK<sub>α</sub> radiation),  $B$  is the peak full width at half maximum and  $\theta$  is the Bragg angle. The calculated crystallite size of the alloy is

19.57 nm and the thin film is 12.37 nm. The optical microscopy observations of the alloy (Fig. 9) revealed that, the parent phase has martensite structure at room temperature. The martensite variants and the grain boundaries in the CuAlNi alloy sample are clear. In Figure 9.b, the surface of the thin film is given. The surface of the thin film is smooth, and there is no martensite variants observed at room temperature.

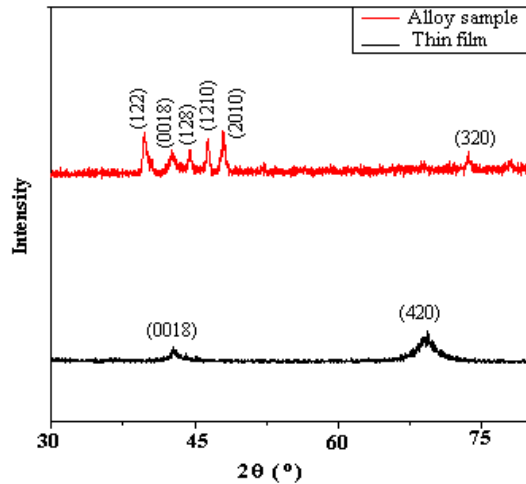


Fig. 8. X-Ray diffraction patterns of the alloy and thin film.

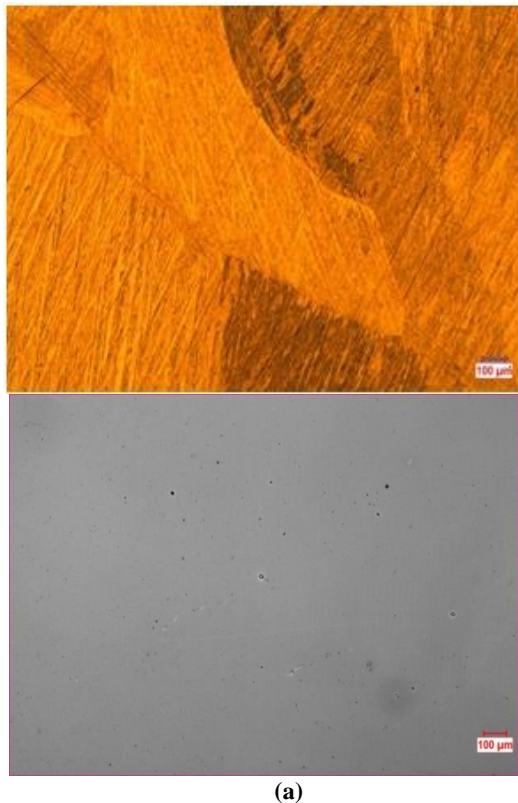


Fig. 9. Optical micrographs of a) alloy and b) thin film.

#### 4. CONCLUSION

The thermodynamical and structural properties of CuAlNi alloy and thin film were investigated. The thermoelastic phase transformations at the ternary CuAlNi SMA system and thin film were observed by heating-cooling processes with DSC analysis. Furthermore, by using different heating and cooling rates to the CuAlNi ternary alloy system, obtained characteristic transformation temperatures and enthalpy values have been found to be changing. The hysteresis value of Af-Ms increased by the increase of heating/cooling rate and the enthalpy changed with the variation of the heating/cooling rate. For the thin film, only M→A transformation was observed and this observation can be detected only one heating/cooling rate. The XRD analysis of the CuAlNi alloy and thin film showed that both of the samples have martensitic structure at room temperature. And this was confirmed with the optical microscope observations for the CuAlNi alloy but we cannot detect any martensitic variants for the thin film.

#### ACKNOWLEDGEMENTS

We are thankful for the financial support by FÜBAP, Project No: FF.12.14.

#### REFERENCES

- Canbay, C. A. (2010). The production of Cu-based shape memory alloys and investigation of microstructural, thermal and electrical properties of alloys, Ph. D Thesis, Fırat University, Institute of Science, Elazığ/Turkey (Turkish).
- Gómez-Cortés, J., J. San Juan, G. López and M. Nó (2013). "Synthesis and characterization of Cu–Al–Ni shape memory alloy multilayer thin films." *Thin Solid Films* Vol. 544, No. pp. 588-592.
- Izadinia, M. and K. Dehghani (2011). "Structure and properties of nanostructured Cu-13.2 Al-5.1 Ni shape memory alloy produced by melt spinning." *Transactions of Nonferrous Metals Society of China* Vol. 21, No. 9 pp. 2037-2043.
- Karagoz, Z. and C. A. Canbay (2013). "Relationship between transformation temperatures and alloying elements in Cu–Al–Ni shape memory alloys." *Journal of Thermal Analysis and Calorimetry* Vol. 114, No. 3 pp. 1069-1074.
- Kato, H., Y. Yasuda and K. Sasaki (2011). "Thermodynamic assessment of the stabilization effect in deformed shape memory alloy martensite." *Acta Materialia* Vol. 59, No. 10 pp. 3955-3964.
- Kissinger, H. E. (1957). "Reaction kinetics in differential thermal analysis." *Analytical chemistry* Vol. 29, No. 11 pp. 1702-1706.
- Lojen, G., I. Anžel, A. Kneissl, A. Križman, E. Unterweger, B. Kosec and M. Bizjak (2005).

"Microstructure of rapidly solidified Cu–Al–Ni shape memory alloy ribbons." *Journal of Materials Processing Technology* Vol. 162, No. pp. 220-229.

Massad, J. E. and R. C. Smith (2005). "A homogenized free energy model for hysteresis in thin-film shape memory alloys." *Thin Solid Films* Vol. 489, No. 1 pp. 266-290.

Meng, Q., H. Yang, Y. Liu and T.-h. Nam (2010). "Transformation intervals and elastic strain energies of B2-B19' martensitic transformation of NiTi." *Intermetallics* Vol. 18, No. 12 pp. 2431-2434.

Otsuka, K. and X. Ren (2005). "Physical metallurgy of Ti–Ni-based shape memory alloys." *Progress in materials science* Vol. 50, No. 5 pp. 511-678.

Otsuka, K. and C. Wayman (1998). "Mechanism of shape memory effect and superelasticity." *Shape memory materials*, No. pp. 27-48.

Ozawa, T. (1970). "Kinetic analysis of derivative curves in thermal analysis." *Journal of Thermal Analysis and Calorimetry* Vol. 2, No. 3 pp. 301-324.

Pérez-Landazábal, J. I., V. Recarte, V. Sánchez-Alarcos, M. L. Nó and J. S. Juan (2006). "Study of the stability and decomposition process of the  $\beta$  phase in Cu–Al–Ni shape memory alloys." *Materials Science and Engineering: A* Vol. 438–440, No. pp. 734-737.

Recarte, V., J. Perez-Landazabal, P. Rodriguez, E. Bocanegra, M. No and J. San Juan (2004). "Thermodynamics of thermally induced martensitic transformations in Cu–Al–Ni shape memory alloys." *Acta materialia* Vol. 52, No. 13 pp. 3941-3948.

Sobrero, C., P. La Roca, A. Roatta, R. Bolmaro and J. Malarria (2012). "Shape memory properties of highly textured Cu–Al–Ni–(Ti) alloys." *Materials Science and Engineering: A* Vol. 536, No. pp. 207-215.

Wang, Z., X. Zu, H. Yu, X. He, C. Peng and Y. Huo (2006). "Temperature memory effect in CuAlNi single crystalline and CuZnAl polycrystalline shape memory alloys." *Thermochimica acta* Vol. 448, No. 1 pp. 69-72.

Xuan, Q., J. Bohong, T. Hsu and X. Zuyao (1987). "The effect of martensite ordering on shape memory effect in a copper-zinc-aluminium alloy." *Materials Science and Engineering* Vol. 93, No. pp. 205-211.

Copyright © Turkish Journal of Engineering (TUJE).  
All rights reserved, including the making of copies  
unless permission is obtained from the copyright  
proprietors.

# Turkish Journal of Engineering



*Turkish Journal of Engineering (TUJE)*  
*Vol. 1, Issue 2, pp. 76-81, September 2017*  
*ISSN 2587-1366, Turkey*  
*DOI: 10.31127/tuje.316696*  
*Research Article*

## **DESIGN AND PROTOTYPE OF A COMPACT, ULTRA WIDE BAND DOUBLE RIDGED HORN ANTENNA FOR BEHIND OBSTACLE RADAR APPLICATIONS**

Betül Yılmaz<sup>1</sup> and Caner Özdemir<sup>\*1,2</sup>

<sup>1</sup>Mersin University, Engineering Faculty, Department of Electrical-Electronics Engineering, 33343 Mersin, Turkey  
(betuly@mersin.edu.tr), (cozdemir@mersin.edu.tr)

<sup>2</sup>Emtech IT Technologies Engineering Corp., Mersin Technology Development Zone, 203, 33343 Mersin, Turkey  
(cozdemir@mersin.edu.tr)

---

\* Corresponding Author

Received: 10/05/2017

Accepted: 26/05/2017

---

### **ABSTRACT**

In this paper, we propose an ultrawide band design for the double ridged horn (DRH) antenna to be used behind the obstacle radar (BOR) applications such as ground penetrating radar (GPR) and through the wall radar (TWR) imaging. The design is developed and optimized by the help of full electromagnetic simulator code; CST. The design parameters such as frequencies of operation and the half power beam width (HPBW) are taken into account by considering the BOR application requirements. The design double ridged horn antenna provides a frequency bandwidth between 1.5 GHz and 7 GHz and HPBW around 30° around the center frequency that are very suitable for GPR and TWR applications. The final optimized design that is formed by CST is physically manufactured and measured. The prototyped DRH antenna's measurement antenna parameter results are in good agreement with the simulated ones.

**Keywords:** *Antenna Design, Ultra-Wide Band Antennas, Double Ridged Horn Antenna and Antenna Measurement*

## 1. INTRODUCTION

High gain, ultra wide band (UWB); but compact antennas have been of great interest for various microwave and radar applications; ranging from electromagnetic compatibility (EMC) measurements to behind the obstacle radar (BOR) detection and localization (Kumar and Ray, 2003; Chair *et al.*, 2004). For such applications, the most important antenna parameters are being the frequency bandwidth and the antenna beam width. The wide frequency bandwidth is usually desired to have as sharp range resolution as possible for applications such as ground penetrating radar (GPR) and through the wall radar (TWR) due to the fact that the object to be detected is in the ranges of a few centimeters (Turk, 2005; Yılmaz and Özdemir, 2016). These applications also require high gain antennas such that the propagated electromagnetic (EM) wave can penetrate opaque obstacles like wall and ground medium. Otherwise, most of the EM energy would be reflected from the air-to-wall or air-to-ground boundary. Another crucial antenna parameter is the width of the main beam along the horizontal plane. For the GPR and TWR usage, the B-scan operation and migration/focusing along the azimuth direction require to have half power beam width (HPBW) values around  $30^\circ$  to  $60^\circ$  for a successful operation of detection and imaging (Yılmaz *et al.*, 2017; Yılmaz and Özdemir, 2017). Above mentioned superior antenna parameter specifications are not possible with conventional antennas like standard gain horns or popular patches such as Vivaldi antennas (Hamid *et al.*, 2011; Uyanik *et al.*, 2016). Horn antennas; for example, have the advantages of providing directive radiation pattern characteristics and high gain features.

On the other hand, they cannot maintain UWB operation as required in GPR and TWR applications (Hamid *et al.*, 2011; Moosazadeh *et al.*, 2016). Vivaldi patch antennas can provide very good UWB frequency usages while they suffer from the gain and the antenna radiation characteristics as in the case of usual patch antennas (Gopikrishnan *et al.*, 2016; Uyanik *et al.*, 2016). To match all these antenna parameter requirements, double ridged horn (DRH) antenna has become a typical solution. While being a type of horn antenna, DRH antenna's ridges inside the plates provide impedance transition structure that is very similar Vivaldi antennas. These translational structures; i.e. ridges, help to match waveguide mode's impedance of  $50 \Omega$  to the air's intrinsic impedance of  $377 \Omega$ . Therefore, DRH antenna is best suited to be a UWB antenna together with high gain and required radiation beam with features.

In this paper, we present our study in designing and prototyping a compact, UWB DRH antenna for BOR applications such as GPR and TWR. In the next section, we share our studies in designing and optimizing the DRH antenna that was aimed to fulfill the specified antenna parameter requirements. The full EM simulation of the designed model is accomplished by the commercially available CST<sup>®</sup> software (URL 1). The designed antenna is optimized successfully to meet the requirements as explained in detail throughout this section. In Sect. 3, the designed DRH antenna is manufactured and measured to be compared with the simulated one. Comparison of the return loss characteristics demonstrates good agreement between the two. The usage of produced DRH antenna is a particular

TWR imaging application is provided with an example. In the final section, the work is summarized.

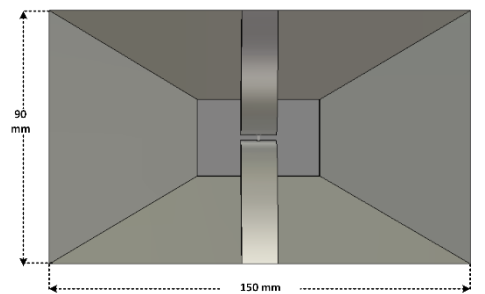
## 2. DESIGN AND THE CST SIMULATION OF DRH ANTENNA

### 2.1. The Design of DRH antenna with CST

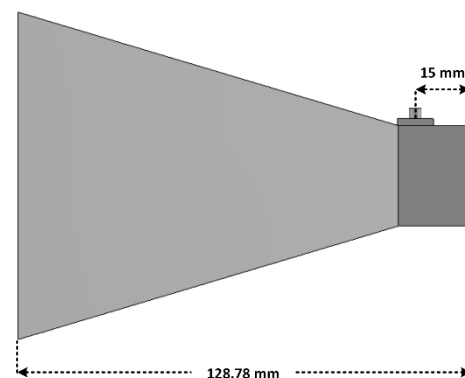
The design and the simulation processes were carried out via full-wave EM simulator code CST. For the design criteria, the frequency of operation for the DRH antenna was chosen to be between 1 GHz and 7 GHz. Another design constraint was the beam of the main lobe and it was aimed to be around  $30^\circ$  to  $45^\circ$  at the center frequency of the bandwidth. The last design parameter was the size of the final designed antenna: Our goal was to have a design with a maximum length to be less than 15 cm.

After carrying out the EM simulations together with optimization runs, we have ended up having the final design as shown in Fig. 1 where the dimensions of the antenna DRH antenna are provided.

In Fig. 1(a), (b) and (c), front, top and perspective views of the designed DRH antenna are shown, respectively. In Fig. 1(d), side view of the inner ridge structure is given with the associated dimensions. As shown from Fig. 1, we ended up with maximum extends of 128.78 mm in length, 150 mm in width and 90 mm in height.



(a)



(b)

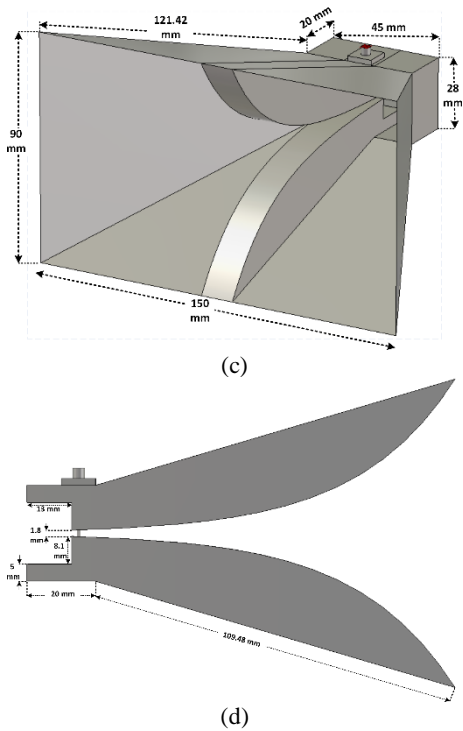


Fig. 1. Designed DRH antenna with dimensions: (a) Front view, (b) side view, (c) perspective view and (d) side view of the ridge.

## 2.2. The Simulation of the Antenna Parameters

Antenna parameters of the designed DRH antenna were simulated by CST simulation software. In Fig. 2, return loss ( $S_{11}$ ) characteristics of the DRH antenna is shown for frequencies. This result yields a -10 dB frequency bandwidth between 1.5 GHz and 7 GHz. Although our first goal was to have a design that can operate between 1 GHz and 7 GHz, we could achieve the about 500 MHz less bandwidth. The reason for sacrificing losing frequencies between 1 GHz and 1.5 GHz is due to size constraint of the design. If we were to include frequencies lower than 1.5 GHz, the antenna was becoming bigger that hardens our employment of antennas to be used BOR applications such as GPR and TWR. Yet, this design is really compact and provides an UWB operation with 78.5% of the total bandwidth (5.5 GHz out of 7 GHz).

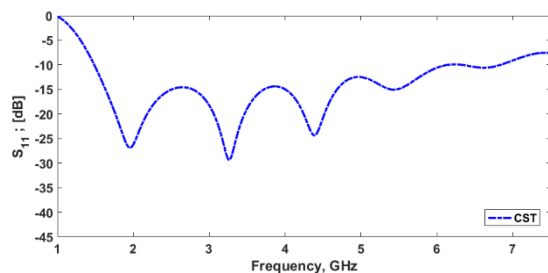


Fig. 2. Return loss plot of the designed DRH antenna

Another important antenna parameter that was considered to be crucial for our BOR applications is the width of the main beam that really affects the detection

success of the target along the azimuth (cross-range) direction. For applications like GPR and TWR, the half power beam width (HPBW) values between  $30^\circ$  to  $45^\circ$  provides a good directivity with sufficient coverage of the possible targets along the azimuth direction.

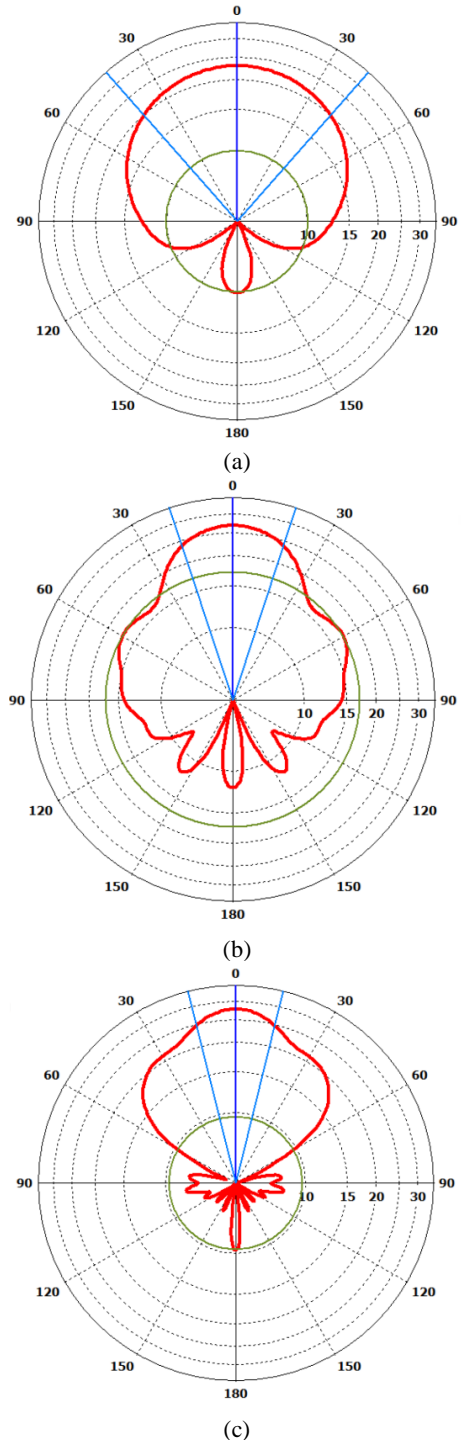


Fig. 3. Azimuth ( $\phi$ ) radiation pattern at elevation angle of  $\theta=90^\circ$  for frequencies; (a) 2 GHz, (b) 4.25 GHz and (c) 7 GHz.

The CST simulation of our designed DRH antenna provides the radiation pattern plots as shown in Fig. 3. In Fig. 3(a), (b) and (c) azimuth polar radiation pattern for

the constant elevation angle of  $90^\circ$  for the lower frequency of 2 GHz, the center frequency of 4.25 GHz and the upper frequency of 7 GHz are given, respectively. As expected, the width of the main beam is larger for lower frequencies, and it becomes narrower as the frequency is increasing. The HPBW of the designed DRH antenna is  $36.5^\circ$  for the mid-frequency of 4.25 GHz that pretty well matches our beam width requirement that we have set at the beginning of this study.

The Gain, HPBW and the side lobe level (SLL) for 2 GHz, 4.25 GHz and 7 GHz are listed in Table 1. As obvious from Fig.3 and Table.1, the maximum side lobe strength is always less than -10 dB for the whole bandwidth. The gain of the antenna ranges from 22.9 dBi to 27.7 dBi that is also satisfactory. Overall the frequency bandwidth results and radiation pattern characteristics of the designed antenna come out to be really suitable to be used in BOR applications.

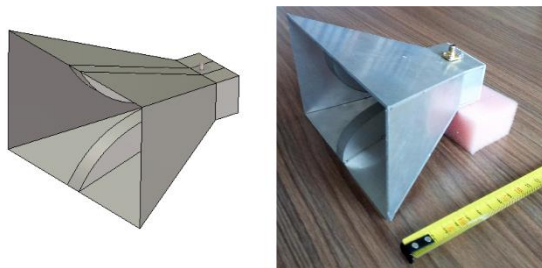
Table 1. Antenna parameters related to radiation pattern of DRH antenna

Frequency	Gain (dBi)	HPBW ( $^\circ$ )	SLL (dB)
2	22.9	82.6	-12.9
4.25	26.8	36.5	-9.7
7	27.7	28	-18.1

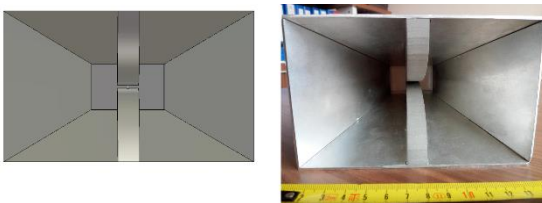
### 3. PRODUCTION AND MEASUREMENT OF DRH ANTENNA

#### 3.1. Prototype of the designed DRH antenna

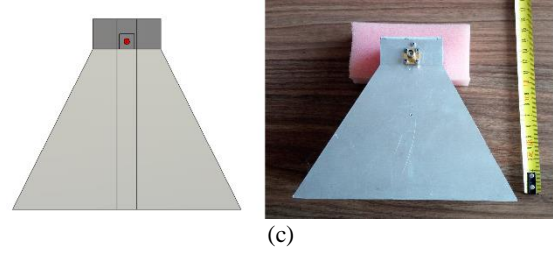
The designed antenna in the previous section was produced by using Aluminum plates of 1 mm thick. Production process was done by an outside company that is professional in cutting, connecting, bonding and welding Aluminum materials. The antenna is fed by an  $50\Omega$  SMA connector as considered during the design. In Fig. 4(a), (b) and (c), the perspective, front and top views of the designed and the produced DRH antenna are shown.



(a)



(b)



(c)

Fig. 4. The designed and produced DRH antenna: (a) perspective view, (b) front view, and (c) top view.

#### 3.2. Measurement of the prototyped DRH antenna

The produced antenna has been put through S11 measurement process in our anechoic chamber at Mersin University's Advanced Research Center. During the measurement, Agilent 5071B ENA Vector Network Analyzer has been used for the return loss measurement for the produced DRH antenna. In Fig. 5, both the measured (shown as red, solid line) and simulated (plotted as blue, dashed line) S11 characteristics are plotted. It is clear from the figure that the agreement between the simulated and the measured return loss is satisfactory. The small discrepancies are due to imperfectness construction of the produced antenna. Overall, the S11 pattern of the prototyped antenna generally follows that of the designed one as the frequency varies within the bandwidth. The measured antenna's lower operation frequency occurred to be around 1.2 GHz that is better than the designed one. On the other hand, the return loss exceeds the lower limit of -10 dB in some frequency regions around 5 GHz and 6 GHz as obvious from the figure.

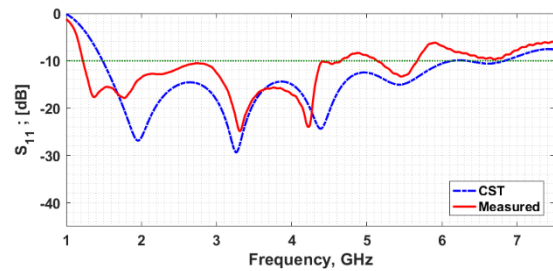


Fig. 5. The return loss results versus frequency: Simulation of designed antenna (dashed, blue) and measurement of produced antenna

#### 3.3. Employment of produced DRH antenna in TWR usage

After completing the design and the prototype studies for our compact DRH antenna, we have produced three copies of the same antenna to be used in TWR application. To demonstrate the usage of these produced antennas, a real experimental scenario has been prepared. A picture of this experimental set-up is shown in Fig. 6. As it can be seen from the figure, three of produced DRH antennas have been connected to a RF transceiver; one being the transmitter and two being the receivers. The RF transceiver has been powered by a portable battery. The control and the automation of the whole system have been

accomplished by a laptop computer. The system produces range-time signatures by two channels with two receiving DRH antennas. After two different range-time signatures are collected, the final image is constructed in range-cross range domain by applying a focusing algorithm.

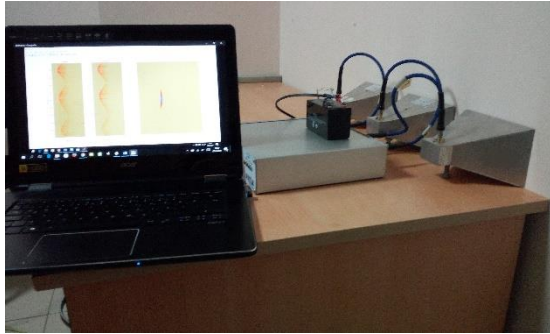


Fig. 6. Experimental set-up with produced DRH antennas for TWR imaging application

By using the set-up in Fig. 6, a measurement has been taken from a case where a man is walking on the other side of the wall while the system was collecting the scattered EM signal. For this particular scenario, the man walked towards and away from the wall for 3 times. In Fig. 7(a), range-time TWR signature histories for one-channel is given. In this image, we can see the characteristic sinusoidal behavior in TWR applications when the target is moving toward and away from the wall. After using the range-time signatures from both channels, the image is focused in range-cross range plane as plotted in Fig. 7(b). This figure shows the real-time location of the human behind the wall in range-cross range domain.

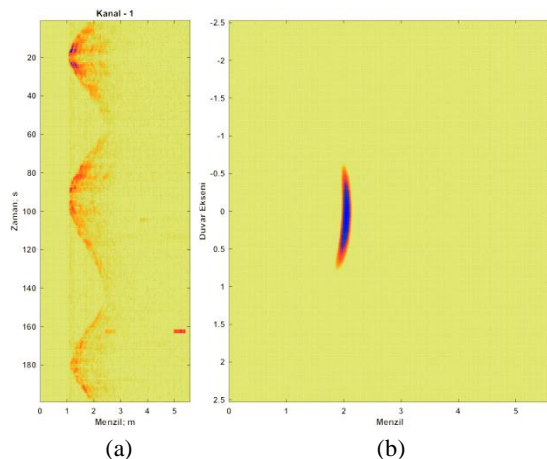


Fig. 7. TWR images obtained by produced DRH antennas: (a) Range-time image, (b) Range-cross range image

#### 4. CONCLUSION

In this study, we have proposed a compact design of DRH antenna structure for ultra-wide band operation and large beam width to be used in behind-the-obstacle radar (BOR) applications. The design is developed in CST simulation program and optimized to match the frequency

bandwidth and radiation pattern beam width requirements. Finalized design of DRH antenna is produced and the prototyped antenna is measured. Simulation and the measured results of return loss characteristics for our compact DRH antenna demonstrate the achievement of this study. Employment of the designed and produced antenna to a real BOR application has verified the successful operation of these antennas.

#### ACKNOWLEDGEMENTS

This work is supported by the Scientific and Research Council of Turkey (TUBITAK) under grant no: TEYDEB-7151335.

#### REFERENCES

- Kumar, G. and Ray K. P. (2003). *Broadband microstrip antennas*, Artech House Inc., Boston.
- Wong, K. (2002). *Planar antennas for wireless communications*, Wiley-Interscience, New York, USA.
- Cai, Y., Guo, Y. J. and Bird, T. S. (2012). "A frequency reconfigurable printed yagiuda dipole antenna for cognitive radio applications." *IEEE Transactions on Antennas and Propagation*, Vol. 60, No. 6, pp. 2905-2912.
- Chair, R., Kishk, A. A. and Lee, K. F. (2004). "Ultrawide-band Coplanar Waveguide-Fed Rectangular Slot Antenna." *IEEE Antennas and Wireless Propagation Letters*, Vol. 3, No. 1, pp. 227-229.
- Turk, A. S. (2005). "UWB performance analysis of PDTEM horn antenna designed for multi-sensor adaptive hand-held GPR." *11th International Symposium on Antenna Technology and Applied Electromagnetics, ANTEM 2005*, St. Malo, France, pp. 1 – 4.
- Nayak, R., Maiti, S. and Patra, S. K. (2016). "Design and simulation of compact UWB Bow-tie antenna with reduced end-fire reflections for GPR applications." *2016 International Conference on Wireless Communications, Signal Processing and Networking, WiSPNET, Chennai, India*, pp. 1786-1790.
- Feng, H., Guofu, Z., Xiaotao, H. and Zhimin, Z., (2010). "Detection of human targets using ultra-wide band through-the-wall radar." *2010 International Conference on Microwave and Millimeter Wave Technology, ICMWT 2010*, Chengdu, China, pp. 1750-1753.
- Yılmaz, B. and Özdemir, C. (2016). "Design and prototype of radar sensor with Vivaldi linear array for through-wall radar imaging: an experimental study." *Journal of Applied Remote Sensing*, Vol. 10, No. 4, pp. 046012:1 -15.
- Yılmaz, B., Özdemir, C. and Akdağlı, A. (2017). "Detection and Localization of a Moving Person behind the Wall based on Bilateralization Technique." *Int. Journal of Electrical and Electronics Engineering (IJEET)*, Vol. 6, No. 1, pp. 2278-9944.
- Yılmaz, B. and Özdemir, C. (2017). "A Detection and Localization Algorithm for Moving Targets behind Walls

based on one Transmitter-two Receiver Configuration.”  
*Microwave Opt. Tech. Letters*, Vol. 59, No. 6, pp. 1252–1259.

Hamid, M. R., Gardner, P., Hall, P. S., and Ghanem, F. (2011). “Switched-band vivaldi antenna.” *IEEE Transactions on Antennas and Propagation*, Vol. 59, No. 5, pp. 1472-1480.

Moosazadeh, M., Kharkovsky, S., Case, J. T and Samali, B. (2016). “Antipodal Vivaldi antenna with improved radiation characteristics for civil engineering applications.” *IET Microwaves, Antennas & Propagation*, Vol. 11, No. 6, pp. 796-803.

Gopikrishnan, G., Zubair A. and Akhtar, M. J. (2016). “A novel corrugated four slot Vivaldi antenna loaded with metamaterial cells for microwave imaging.” *2016 Asia-Pacific Microwave Conference, APMC, New Delhi, India*, pp. 1-4.

Uyanik, C., Dalgıç, Ö., Ertay, A. O., Doğu, S., Çayören, M. and Akduman, İ. (2016). “Design of Slotted Vivaldi antenna for microwave imaging applications.” *2016 National Conference on Electrical, Electronics and Biomedical Engineering, ELECO 2016, Bursa, Turkey*, pp. 547 – 549.

URL 1, CST: Computer Simulation Technology, Studio Suite website, <https://www.cst.com/> [Accessed 26.05.2017].

Copyright © Turkish Journal of Engineering (TUJE).  
All rights reserved, including the making of copies  
unless permission is obtained from the copyright  
proprietors.

# Turkish Journal of Engineering



*Turkish Journal of Engineering (TUJE)*  
*Vol. 1, Issue 2, pp. 82-87, September 2017*  
*ISSN 2587-1366, Turkey*  
*DOI: 10.31127/tuje.316675*  
*Research Article*

## **PHOTOGRAMMETRIC MODELLING OF SAKAHANE MASJID USING AN UNMANNED AERIAL VEHICLE**

Ahmet Şasi \*<sup>1</sup>, Murat Yakar <sup>2</sup>

<sup>1</sup> Selçuk University, Faculty of Engineering, Department of Geomatics Engineering, Konya, Turkey  
(sasiahmet@gmail.com)

<sup>2</sup> Mersin University, Faculty of Engineering, Department of Geomatics Engineering, Mersin, Turkey  
(myakar@mersin.edu.tr)

---

\* Corresponding Author

Received: 10/05/2017

Accepted: 28/05/2017

---

### **ABSTRACT**

Turkey has been home to various cultures and civilizations throughout history. Thus, it is a piece of land that has architecturally maintained the cultural structure of civilizations throughout history. This geography we live in served as a capital to many civilizations to this date. Considered as the birth place of civilization, the Anatolian soils historically accommodated many civilizations. To this end, Konya served as the capital of Anatolian Seljuk Empire between 1086 and 1308. Ergo, this geography houses a vast accumulation of cultural and historical heritage. We owe history a debt to show necessary effort in order to pass down these cultural assets that survived throughout history to future generations. Therefore, documentation and protection of cultural assets are important for them to be passed down from one generation to the other. This article discusses the 3D photogrammetric modelling of Sakahane Masjid from the Anatolian Seljuk Empire era, located in Ferhuniye Neighborhood in Konya Province. A Nikon D90 Camera and DJI Phantom 4 Unmanned Aerial Vehicle were used in taking photographs of the historical artifact for the purposes of 3D photogrammetric modelling. DJI Go 4 and Pix4Dcapture mobile applications were used to capture photographs using the unmanned aerial vehicle. The data obtained were evaluated via Agisoft PhotoScan software and 3D models of the artifact were acquired. The 3D model of the said cultural asset is meant to be a resource for future generations in terms of the protection of cultural heritage. It is foreseen that this model will also provide an opportunity for a faithful restoration in case of any possible damage to this historical artifact, as well as offering solutions to the problems of many professional disciplines today.

**Keywords:** *Unmanned Aerial Vehicle, 3D Modelling, Photogrammetry, Historical Artifact, Cultural Heritage*

## 1. INTRODUCTION

The geography we live in has been home to many different cultures and civilizations. Various societies sustained their lives on this soil as part of the said cultures and civilizations. These societies that lived on this land throughout history built assets reflecting their own cultures. These assets, the legacy of history to us, are defined as Cultural Assets. Protecting cultural assets is a duty of mankind in order to display ownership of universal assets and sustain the history. Documentation practices bear a great importance for historical development and protection of cultural assets, as they are aimed at documenting cultural heritage in order to display ownership of the historical values we inherited and make contributions to world heritage.

Cultural and natural heritage face the gradually-growing danger of deperdition due to natural and unnatural causes. Countries with cultural and natural heritage fall short of protecting such heritage owing to a lack of economic, scientific and technical resources. Thus, it is the duty of all nations to share scientific studies and recent techniques for the protection of such cultural heritage. Turkey has been home to various cultures and civilizations, and it showcases the cultural heritage passing down from these civilizations. It is as important for the world cultural heritage as it is for our country to protect these artifacts by meticulously documenting them (Yakar, M., 2011).

Today, documentation procedures for cultural assets can be performed quickly, accurately and in a reliable way thanks to the photogrammetry technique. Since cultural assets have elaborative and detailed architecture, it is necessary to employ state-of-the-art measurement tools and techniques for the documentation of cultural heritage. The 3D model obtained via digital photogrammetry technique can be used in many disciplines. It can be a resource for many professional disciplines in order to come up with solutions to problems that may occur in the future.

In this study, however, the aerial photogrammetry technique was used. Terrestrial photogrammetry technique was also employed to complement aerial photogrammetry. Aerial shots of the cultural asset were taken by unmanned aerial vehicle (UAV) while the facades of the artifact were photographed with a Nikon D90 camera. Tie points were used to link together and relate aerial and terrestrial photographs of the artifact, and a 3D model was then obtained. The study aimed at rendering the 3D model obtained from this study a resource for faithful restoration of the cultural asset following possible future damages, contributing to the promotion of the city as well as the country and, most importantly, protecting and passing down the cultural heritage to future generations.

Since photographs were taken from different altitudes and camera angles above the asset to get a 3D model of the artifact, it is also aspired that this study will serve as a model and guide for upcoming studies as regards the points to be mindful of while creating a 3D model.

## 2. PROTECTION AND DOCUMENTATION OF CULTURAL ASSETS

Today, there are studies and products that can set the basis for the restoration of the cultural assets we have in our country in the case of damages to and partial or total destruction of cultural assets due to natural disasters such as earthquakes and fire as well as providing new research opportunities for other disciplines. The 3D models obtained via photogrammetry technique constitute an accurate point of reference for administrators of the city and the country alike, facilitating their decision-making process.

The information to be obtained from documentation studies towards the protection of cultural heritage needs to be organized in a way that it will be understood and used by specialists from different disciplines that are to take part in the protection of documents having a variable quality and quantity. Metric, written and visual documentation can be used as baseline data for the determination of current status and problems of cultural heritage and for all protection studies regarding the solutions to these problems, and they are also a way of passing down the cultural heritage to future generations and promoting cultural heritage within the society (Yakar, M., 2015).

The documentation and 3D modelling of cultural assets, the integration of all information on attributes and features through these studies and the employment of cutting-edge technologies to do this contribute to the development of history, the world cultural heritage and the publicity of the city as well as tourism, technology and science within the country.

## 3. FIELD OF STUDY

### 3.1. Sakahane Masjid

Sakahane Masjid is the second cultural asset for which a 3D model is prepared. It is located in Sultan Mesut Street of Ferhuniye Neighborhood in Selçuklu District of Konya Province. The coordinates of Sakahane Masjid, a Cultural Asset, are 37°52'30.31" N latitude and 32°29'29.11" E longitude.

It was built by Emir Kemaleddin in 1248 during the era of Anatolian Seljuk Empire. The artifact was registered by Konya Regional Board of Cultural Heritage Protection on November 13, 1982. It was originally built as a masjid and is still used for the same purpose (Gümüş, H., Koçak, F., 2010).

Some research studies suggest that this masjid was the masjid of Konya Alaeddin Darüşşifa (Hospital). The artifact is made up of rubble stone and bricks. The masjid has a square plan with four walls made up of bricks and stone. Rising on these walls is a small brick dome which was later covered with lead. The Turkish triangle was used as pendentive at zones of transition to the dome (Gümüş, H., Koçak, F., 2010).

Sakahane Masjid is also called Şifahane (Hospital). Research shows that it is also named Hızır İlyas Masjid in historical resources.

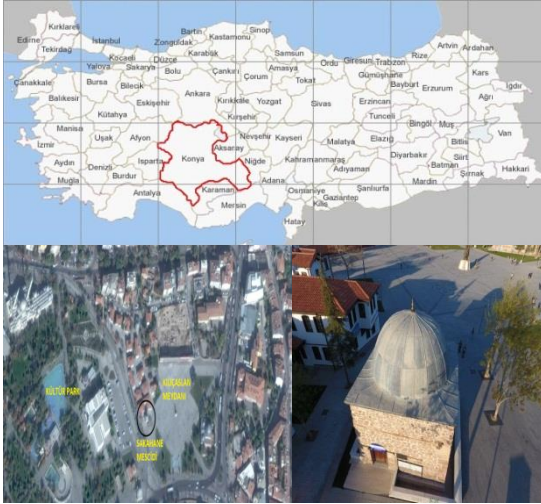


Fig. 1. Location of Sakahane Masjid

### 3.2. Technical Equipment and Software Used in the Study

For the 3D modelling of cultural assets, a Nikon D90 camera and a DJI Phantom 4 unmanned aerial vehicle were used to capture images. For flying the unmanned aerial vehicle, the DJI Go 4 mobile application was utilized. Weather conditions were monitored via UAV Forecast mobile application to ensure favorable weather conditions were present for flight.



Fig. 2. Nikon D90 camera and DJI Phantom 4 unmanned aerial vehicle

Agisoft PhotoScan software was used for the photogrammetric evaluation of the photos taken.

### 3.3. Photogrammetric Evaluation

In this 3D modelling of the cultural asset, we employed the photogrammetry technique using a DJI Phantom 4 UAV. Moreover, in order to obtain better results from the modelling of the artifact's facades, the terrestrial photogrammetry technique was used with the help of a Nikon D90 camera.

The 3D modelling of Sakahane Masjid via the photogrammetry technique was carried out through field surveys and desktop work. In field surveys, cultural heritage sites were terrestrially and aerially photographed. Since aerial photographs taken with the

DJI Phantom 4 contain latitude, longitude and altitude information thanks to IMU, compass and GPS features of the UAV, the model reflects the true coordinates of the cultural asset.

The software used in the evaluation of the photographs creates a calibration report of the camera used. In order to integrate terrestrial and aerial photographs, tie points were determined and photographs corresponding to these points were aligned and matched. Following the alignment process, all information obtained in field surveys and desktop work via photogrammetric software was evaluated.

#### 3.3.1. Field Survey for Sakahane Masjid

For the sake of flying the unmanned aerial vehicle in the field, firstly, the DJI Phantom 4 unmanned aerial vehicle was registered at the Directorate General of Civil Aviation. Then, a flight permit was obtained from Konya Governor's Office and the district police department was provided with information on the location and time of the flight. All these processes are extremely important in terms of public safety as well as flight safety. After the flight permit was obtained and relevant departments were notified, conditions for a safe flight were ensured. In the field surveys for the 3D modelling of Sakahane Masjid, photographs of the historical artifact were taken thanks to the DJI Go 4 mobile application by manually flying DJI Phantom 4 unmanned aerial vehicle. There is a high level of overlapping among the photographs of the cultural heritage. All photographs of the artifact were taken in line with this principle.

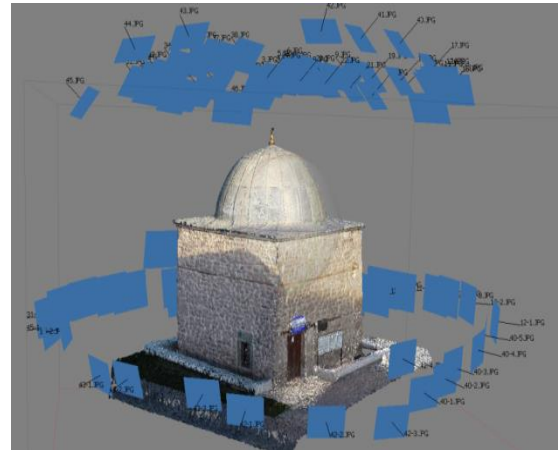


Fig. 3. Overlapping photographs of the artifact

Prior to the flight, UAV Forecast application was used to determine whether the field is fit to fly the unmanned aerial vehicle. This application utilized the information regarding sunrise and sunset time, the speed and direction of the wind, if available, whether the weather is overcast as well as sight distance to determine whether it was a day fit to fly.



Fig. 4. Checking weather conditions for flight

After making sure that the weather conditions were fit for flight, we went on to the field to take photographs. The unmanned aerial vehicle was matched with the DJI Go 4 mobile application prior to the flight. The Compass and IMU of the unmanned aerial vehicle were calibrated. These calibrations are important as they ensure the unmanned aerial vehicle vertically suspends in the air in a stable manner without vibrating.

The Compass is calibrated by rotating the unmanned aerial vehicle 360° around its own axis both horizontally and vertically.

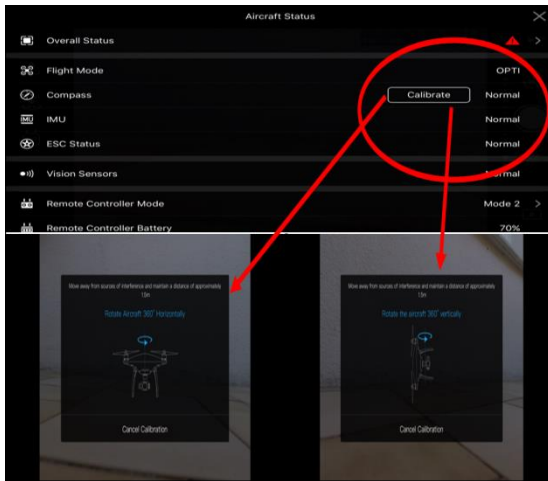


Fig. 5. Calibrating the compass of the unmanned aerial vehicle

The compass calibration was followed by the calibration of the IMU. The IMU helps stabilize the unmanned aerial vehicle especially in windy weather conditions and eliminates drift errors in photographs. The calibration process took approximately 5 minutes.

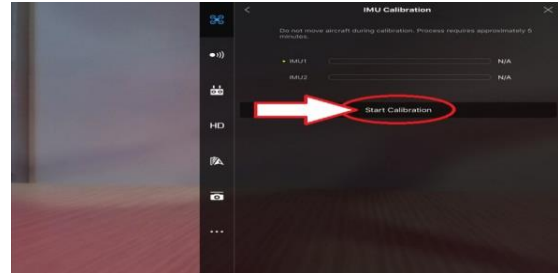


Fig. 6. Calibrating the IMU of the unmanned aerial vehicle

After obtaining the required permits for the field of flight, it was determined that the field of flight was fit for flying the unmanned aerial vehicle. Completing the required IMU and Compass calibrations, we flew the UAV. Photographs of Sakahane Masjed were taken by the manually-controlled unmanned aerial vehicle. Each facade of the cultural heritage was photographed, ensuring a high overlapping rate. Aerial photographs were supported by terrestrial photographs taken with the Nikon D90 camera.



Fig. 7. Aerial photographs of Sakahane Masjed

The accuracy of geographical coordinates of Sakahane Masjed photographs which were taken by the unmanned aerial vehicle was checked via Google Earth. The program allows for conversion into the national coordinate system at a later time. Thus, the final model is produced with coordinates.

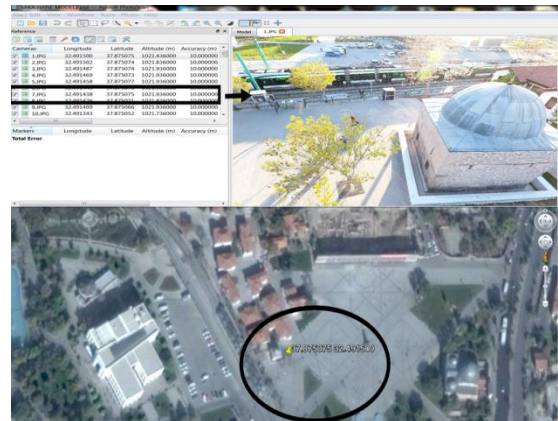


Fig. 8. Consistency of photograph and satellite coordinates

Field surveys for Sakahane Masjid were thus completed. The next stage involved the desktop work regarding the 3D modelling of the cultural assets. Photographs were processed with Agisoft PhotoScan software and the 3D models of the historical artifacts were obtained as an end product.

### 3.3.2. Desktop Work for Sakahane Masjid

Photographs of Sakahane Masjid were evaluated with the Agisoft PhotoScan software. First, the photographs were aligned with a high overlapping rate.

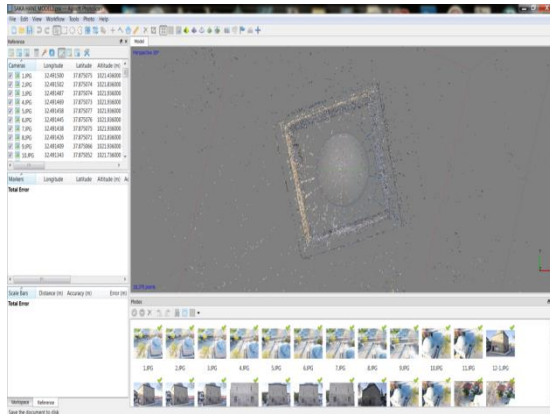


Fig. 9. Alignment of Sakahane Masjid photographs

The aligned photographs helped acquire a point cloud via the high overlapping rate. The second step was to build a dense point cloud. Workflow - Build Dense Cloud – High – Mild option sequence was followed. This process took 8 hours and 7 minutes. As a result, 9,043,919 point clouds were generated.

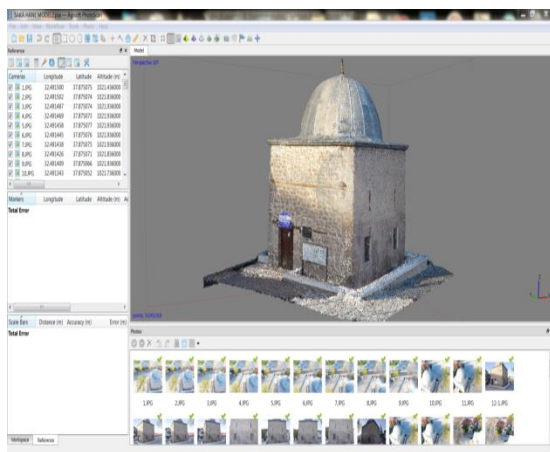


Fig. 10. Building a dense cloud for Sakahane Masjid

Following the completion of building the dense cloud, Workflow-Build Mesh option sequence was followed in order to create a solid model of the dense cloud. Generally, in building modelling, Arbitrary - Dense Cloud - High option sequence was followed and a solid model was obtained by choosing Enabled in Interpolation tab.

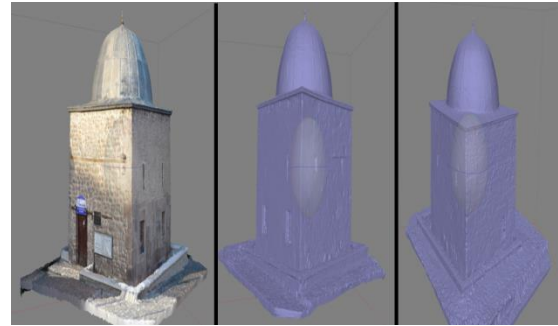


Fig. 11. Solid Model Creation - Build Mesh - Triangle Model (Build Mesh)

Following the Build Mesh process, Workflow - Build Texture option sequence enabled the texture building. In this study, Adaptive Orthophoto (used for vertical texture building) - Mosaic and Enable Color Correction options were used. Following the process, texture building for the solid model was completed.

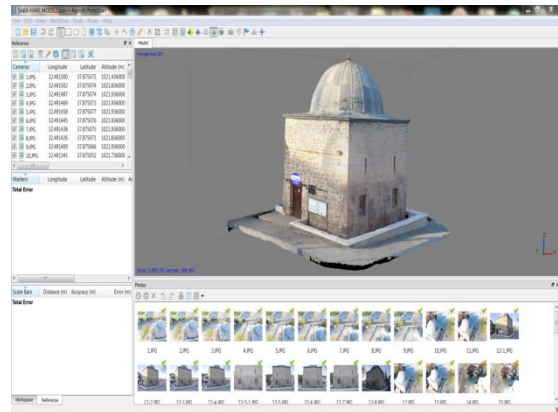


Fig. 12. Texture building for the solid model

In order to obtain a high-quality look for the details and the meshes of the object, the Build Tiled Model option was chosen from the Workflow menu. The 3D model of Sakahane Masjid then involved coordinates.

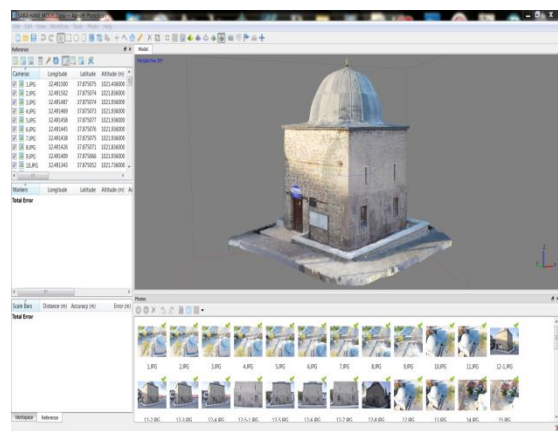


Fig. 13. General view of the 3D model (Build Tiled Model)

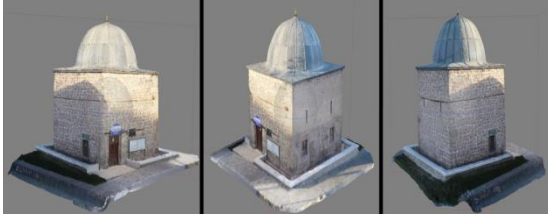


Fig. 14. Facade views of the 3D model (Build Tiled Model)

#### 4. FINDINGS

During the study, the following issues regarding the creation of better models in 3D modelling via unmanned aerial vehicle were determined.

- There must be an adequate number of oblique photographs of the objects and details in suitable positions regarding the objects for which 3D models will be produced. Photographs must be taken in a way to ensure a high overlapping rate.
- It is preferable to take the photographs when the sun is close to setting or after the sun rises in order for the artifact not to be shadowed. This way, the modelled artifact cannot have one shady facade while another one is bright.
- The ambient amount of light around the artifact to be modelled should be sufficient. Details of the artifact cannot be seen clearly under dark and insufficient ambient light.
- Attention should be paid to homogeneously distributing the tie points on the object which are placed in order to relate the photographs to each other.
- It is of crucial importance for 3D modelling that the alignment of photographs is done with a high overlapping rate via Agisoft PhotoScan software.
- During the densification of the point cloud obtained through alignment of the photographs, the densest point setting should be selected while the mild setting be opted for in building modelling.

#### 5. CONCLUSION

In this study, 3D models of Sakahane Masjid, which is located in Ferhuniye Neighborhood of Selçuklu District in Konya Province, were produced. The 3D modelling consists of two stages, namely field survey and desktop work. A Nikon D90 camera and a DJI Phantom 4 unmanned aerial vehicle were used to take photographs of the historical artifacts. Photographs taken were evaluated with Agisoft PhotoScan software. Since the photographs taken by unmanned aerial vehicle contain geographical coordinates, the model also involved the information on coordinates.

This 3D model belongs to a historical artifact which has survived since the era of the Anatolian Seljuk Empire and bears an important historical value for our country. It is a significant cultural asset for both our country and state. Thus, I intend that this study emerges as a future resource for both our country and the world cultural heritage for a faithful restoration of such historical artifacts. This study constitutes a reliable and accurate resource for faithful restoration practices against deformation that might be observed in relation to the historical artifact due to possible natural disasters or

physical interventions.

The study we have conducted also contributed to creating documentation on cultural assets across the country.

#### ACKNOWLEDGEMENTS

I would like to thank Prof. Murat YAKAR, my advisor, for sharing his knowledge and experience with me and for encouraging me to be a part of and contribute to documentation studies for cultural assets.

#### REFERENCES

- Gümüş, H., Koçak, F., (2010). "Inventory of Immovable Cultural and Natural Heritage of Konya Province." *Konya Metropolitan Municipality, Archive for Immovables.*
- Uysal, M., Toprak, A.S., Polat N. (2013). "3D Photogrammetric Modelling of Afyon Gedik Ahmet Pasha(Imaret) Mosque." *TNPRSA Technical Symposium VII, Trabzon.*
- Yakar, M., (2015). "Surveying Sample of Sahip Ata Social Complex." *UCTEA Chamber of Survey and Cadastre Engineers, 10th Turkish Scientific and Technical Congress on Geomatics.*
- Yakar, M., Çetin, M., Yıldız, F., Metin, A., Uray, F., Kahya, İ., Çiçek, V. "3D Modelling and Animation of Italian Catholic Church of Mersin." *UCTEA Chamber of Survey and Cadastre Engineers, 13th Turkish Scientific and Technical Congress on Geomatics, April 18-22, 2011, Ankara*
- Yakar, M., Yılmaz, H.M. (2008). "Photogrammetric Surveying Study and 3D Modelling for Horozluhan, a Historical and Cultural Heritage." *S.U. Fac. Eng.-Arch. Magazine Issue: 23 P.2: 25 – 33*
- Web Map Tile Service, 7. [www.agisoft.com](http://www.agisoft.com) [Accessed 15 Apr 2017].
- Web Map Tile Service, 7. [www.dji.com](http://www.dji.com) [Accessed 15 Apr 2017].
- Web Map Tile Service, 7. <https://pix4d.com/> [Accessed 15 Apr 2017].
- Web Map Tile Service, <https://tr.wikipedia.org> [Accessed 10 May 2017].

Copyright © Turkish Journal of Engineering (TUJE). All rights reserved, including the making of copies unless permission is obtained from the copyright proprietors.

## CONTENTS



MINERALOGICAL, GEOCHEMICAL AND MICROMORPHOLOGICAL CHARACTERISTICS OF CALCITE PRECIPITATED FROM A THIN COVER OF RECENT WATER TAKEN FROM THE STALAGMITES IN KÜPELI CAVE, ESENPINAR (ERDEMLI, MERSIN), SOUTHERN TURKEY  
Muhsin Eren, Selahattin Kadir and Murat Akgöz ..... 44

REGRESSION MODELING OF THE HOLE QUALITIES DURING COLD WORK TOOL STEELS DRILLING, WITH DIFFERENT CHARACTERISTICS DRILL BITS  
İskender Özkul, Berat Barış Buldum and Adnan Akkurt ..... 52

THE INVESTIGATION ON ELECTRICAL AND OPTICAL PROPERTIES OF CdO/CNT NANOCOMPOSITE  
Ömer Guler, M. Gökhan Albayrak, Mehmet Takgün and Seval Hale Güler... 61

DESIGNING A COMPACT MONOPOLE MICROSTRIP ANTENNA OPERATING AT ULTRA-WIDE BAND FOR MICROWAVE IMAGING APPLICATIONS  
Mustafa Berkan Biçer and Ali Akdağlı ..... 66

FABRICATION OF Cu-Al-Ni SHAPE MEMORY THIN FILM BY THERMAL EVAPORATION  
Canan Aksu Canbay, Ayşe Tekataş and İskender Özkul..... 70

DESIGN AND PROTOTYPE OF A COMPACT, ULTRA WIDE BAND DOUBLE RIDGED HORN ANTENNA FOR BEHIND OBSTACLE RADAR APPLICATIONS  
Betül Yılmaz and Caner Özdemir..... 76

PHOTOGRAMMETRIC MODELLING OF SAKAHANE MASJID USING AN UNMANNED AERIAL VEHICLE  
Ahmet Şasi, Murat Yakar..... 82

ISSN 2587-1366

# TURKISH JOURNAL OF ENGINEERING